AIMS Mathematics, 11(11): 38109–38140.
DOI: 10.3934/math.20261472
Received: 31 August 2026
Revised: 13 October 2026
Accepted: 21 October 2026
Published: 16 November 2026

https://www.aimspress.com/journal/Math

Research article

Inversion-based adaptive control for uncalibrated visual servoing of robotic manipulators with actuator backlash

Rong Lu[1], **Jianlan Guo**[2,*], **Guanyu Lai**[3], **Haoxu Shi**[4] **and Xiaohang Su**[3]

[1] School of Artificial Intelligence, Dongguan Polytechnic, Dongguan 523808, China
[2] School of Electronic Information, Dongguan Polytechnic, Dongguan 523808, China
[3] School of Automation, Guangdong University of Technology, Guangzhou 510006, China
[4] Faculty of Innovation Engineering, Macau University of Science and Technology, Taipa, Macau 999078, China

* **Correspondence:** Email: guojl@dgpt.edu.cn.

Abstract: This work studied single-point image-space regulation for robotic manipulators with unknown camera parameters and asymmetric actuator backlash. Unequal branch gains introduce direction-dependent compensation errors into the visual feedback loop. A smooth asymmetric inverse was incorporated into the torque controller, with the branch-slope ratio assumed known. Its compensation error was separated into a linearly parameterized component and a bounded residual. An adaptive inverse and a robust adaptive term addressed these components in parallel, while the camera parameters were updated online. The Lyapunov analysis established boundedness and the vanishing joint velocity on the stated operating domain. The joint configuration and image error had finite limits, with zero image error following under the specified feedback-rank and net-residual conditions. Simulations on a three-joint model based on the PUMA 560 parameterization illustrated the regulation performance. Supplementary tests assessed sampled visual feedback, delay, noise, camera estimation, and the effects of the compensation modules.

Keywords: adaptive control; manipulators; actuator backlash; visual servoing; nonlinear systems
Mathematics Subject Classification: 93C40, 93C85, 93D20

1. Introduction

Control of robotic manipulators has been studied for a range of applications [1–3]. Visual servoing uses image measurements to guide robot motion. Its two main formulations are position-based visual servoing (PBVS) and image-based visual servoing (IBVS). PBVS defines the control error using an estimated pose in Cartesian space [4, 5]. IBVS defines the error directly from image features, such as

pixel coordinates, without explicitly reconstructing the target pose [6–8]. Conventional model-based IBVS depends on an accurate image Jacobian, which is generally obtained through camera calibration. The calibration requirements have motivated uncalibrated IBVS methods [9–11].

Kinematics-based approaches estimate the relation between robot motion and image measurements [10–12]. Filtering and neural-network estimators have been used to update this relation online [11]. A zeroing neural network has also been applied to data-driven image-based visual servoing [12]. These methods describe the motion–image relation at the kinematic level. For torque-controlled manipulators, incorporating the robot dynamics allows the control law to account for the mechanical response [13–15].

Dynamics-based methods estimate unknown parameters within the visual feedback loop. Depth adaptation was investigated in [14], while the depth-independent interaction matrix in [15] avoids explicit depth measurement under ideal actuation. Further developments include joint estimation of kinematic and camera parameters [16] and formulations using uncalibrated stereo cameras [17]. These studies addressed uncertainty in the visual and kinematic models. Practical actuators may also exhibit a dead zone [18, 19], saturation [20, 21], backlash [22–24], and hysteresis [25–27]. Such nonlinearities alter the relation between commanded and transmitted torque and must be accounted for in the visual control loop.

Related control studies have considered optimal control with unknown dynamics and actuator saturation [28], performance recovery under denial-of-service attacks [29], and predefined-time formation control under deception attacks [30]. These studies address actuator uncertainty and feedback disruptions in different control settings.

Backlash introduces dependence on motion direction and the stored actuator output, so the transmitted torque depends on the input history. Tao et al. [31] developed a nonsmooth backlash inverse with adaptive updates for symmetric backlash. Zhou et al. [32] subsequently studied smooth inverse compensation. Wang et al. [33] incorporated this approach into adaptive robust visual servoing with symmetric backlash. Asymmetric backlash has also been considered in geared transmission control [34]. Unequal branch gains introduce a directional mismatch in inverse compensation. When the camera parameters are also unknown, the associated actuator errors must be handled together with the visual-model uncertainty.

For robotic manipulators, prescribed-performance designs have been developed for predefined-time reliable control [35] and fixed-time control with input saturation [36]. These results motivate further work on transient-performance specifications in uncalibrated visual servoing. The present study considers asymptotic image regulation under the conditions established below.

We address this problem using a smooth asymmetric inverse within an uncalibrated visual-servoing controller. The slope ratio $r = m_r/m_l$ is assumed known, making the selected regressor computable. The absolute slopes and backlash offsets remain unknown and are represented by the parameters estimated online. The contributions are summarized as follows:

1. A smooth inverse that retains the unequal branch gains is incorporated into the torque controller. The directional gain difference is preserved in the inverse and its compensation-error expression.
2. The compensation error is separated into a linearly parameterized component and a bounded residual. Parameter adaptation and adaptive robust compensation address these components in parallel.

3. The analysis establishes boundedness and finite limits of the joint configuration and image error on the stated operating domain. It relates the limiting image error to the net residual torque and specifies the feedback-rank and residual conditions for convergence to zero.

2. Problem statement

We consider visual servoing of a manipulator with asymmetric actuator backlash using a fixed, uncalibrated camera. The objective is to regulate the image coordinates of a single feature point on the end effector to a constant desired value. Figure 1 shows the system configuration.

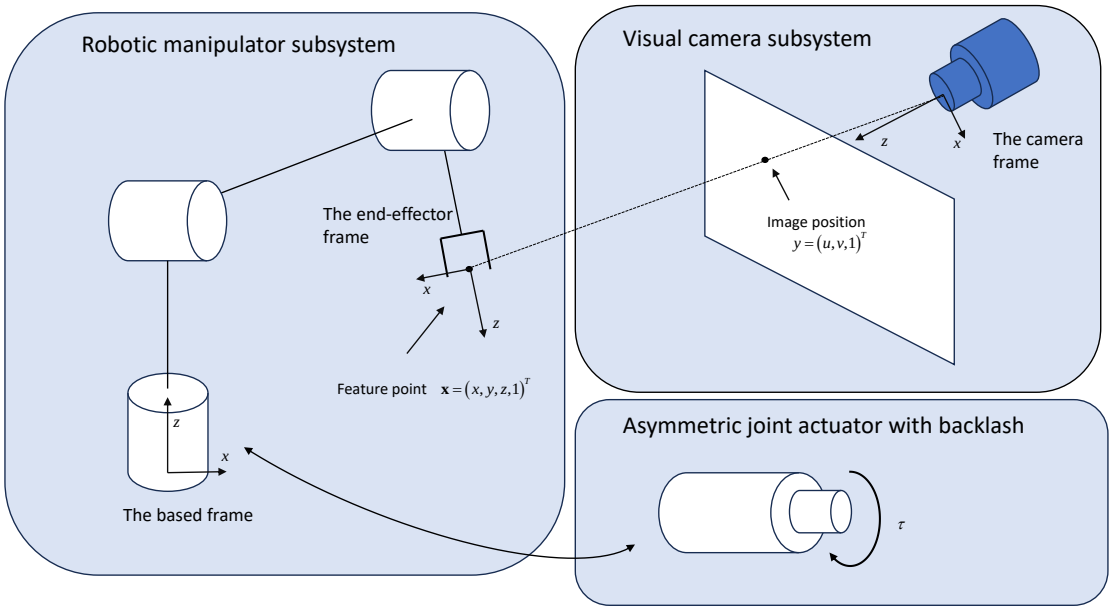


Figure 1. The basic structure of the visual servoing system.

2.1. The kinematics model

To delineate the system, we establish three coordinate frames: The base frame, the camera frame, and the end-effector frame. The space position of the feature point is represented by $\boldsymbol{x}(\mathrm{t}) \in \mathbb{R}_{4\times1}$. By utilizing transformation matrix $\boldsymbol{T}$ to obtain the camera coordinates, the transformation formula is given as

$$^{c}\boldsymbol{x}(t) = \boldsymbol{T}\boldsymbol{x}(t), \tag{2.1}$$

where $\boldsymbol{T}$ is a matrix involving extrinsic camera parameters. Let a vector $\boldsymbol{q}(t) \in \mathbb{R}_{n\times1}$ represent the robotic joint position. The joint angles $\mathbf{q}(t)$ and the space position have the following relationship:

$$\dot{\boldsymbol{x}}(t) = \boldsymbol{J}\dot{\boldsymbol{q}}(t), \tag{2.2}$$

where $\boldsymbol{J} = \frac{\partial \boldsymbol{x}(\mathrm{t})}{\partial \boldsymbol{q}(t)}$ denotes the manipulator Jacobian matrix. The image coordinates representing the image projection are given as

$$\boldsymbol{y}(t) = \begin{pmatrix} u(t) & v(t) & 1 \end{pmatrix}^T. \tag{2.3}$$

Based on the pinhole camera model, the perspective projection maps the base coordinates onto the image coordinates. The corresponding model is formulated as follows:

$$\boldsymbol{y}(t) = \frac{1}{{}^{c}z(t)}\boldsymbol{M}\boldsymbol{x}(\mathrm{t}), \tag{2.4}$$

and ${}^{c}z(t)$ is rewritten as

$${}^{c}z(t) = \boldsymbol{m}_3^T\boldsymbol{x}(\mathrm{t}), \tag{2.5}$$

where $\boldsymbol{M} \in \mathbb{R}_{3\times4}$ represents the projection matrix, ${}^{c}z(t)$ represents the depth value of the feature point relative to the camera coordinate origin, which is positive, and $\boldsymbol{m}_3^T$ represents the third row of $\boldsymbol{M}$. $\boldsymbol{M}$ must have a full rank only and can be scaled by arbitrary proportional factors. Then

$$\boldsymbol{y}(t) = \frac{\boldsymbol{M}\boldsymbol{x}(\mathrm{t})}{\boldsymbol{m}_3^T\boldsymbol{x}(\mathrm{t})} = \frac{\beta\boldsymbol{M}\boldsymbol{x}(\mathrm{t})}{\beta\boldsymbol{m}_3^T\boldsymbol{x}(\mathrm{t})}. \tag{2.6}$$

This property demonstrates that the projection is invariant to scaling the matrix $\boldsymbol{M}$ by any non-zero constant β. Consequently, the projection matrix $\boldsymbol{M}$ is only defined up to a scale factor and is therefore not unique. Based on this property, it is known that the solution is not unique. Therefore, by fixing a variable of $\boldsymbol{M}$, the other 11 variables can be estimated by an adaptive rule. They are listed in a vector denoted by $\boldsymbol{\vartheta}$:

$$\boldsymbol{\vartheta} = (m_{11}, m_{12}, m_{13}, ..., m_{32}, m_{33})^T, \tag{2.7}$$

where m_{ij} denotes the components of matrix $\boldsymbol{M}$ and $\boldsymbol{\vartheta}$ represents the unknown camera parameter vector, which requires online estimation.

Since the depth information of the uncalibrated monocular camera is both unknown and unmeasurable, the subsequent approach constructs an IBVS controller that does not rely on depth information. Differentiating (2.4) and using (2.5) gives the image velocity

$$\dot{\boldsymbol{y}}(t) = \frac{1}{{}^{c}z(t)}(\boldsymbol{M}\dot{\boldsymbol{x}}(\mathrm{t}) - \boldsymbol{y}(t){}^{c}\dot{z}(t)). \tag{2.8}$$

Incorporated with (2.5), we obtain

$$\dot{\boldsymbol{y}}(t) = \frac{1}{{}^{c}z(t)}\boldsymbol{A}(\boldsymbol{y}(t))\,\dot{\boldsymbol{x}}(\mathrm{t}), \tag{2.9}$$

where $\boldsymbol{A}(\boldsymbol{y}(t)) \in \mathbb{R}_{3\times4}$ is given as

$$\begin{aligned}\boldsymbol{A}(\boldsymbol{y}(t)) &= \boldsymbol{M} - \boldsymbol{y}(t)\boldsymbol{m}_3^T \\ &= \begin{pmatrix} \boldsymbol{m}_1^T - u(t)\boldsymbol{m}_3^T \\ \boldsymbol{m}_2^T - v(t)\boldsymbol{m}_3^T \\ 0 \end{pmatrix}.\end{aligned} \tag{2.10}$$

It should be noted that the matrix $\boldsymbol{A}$ remains unaffected by ${}^{c}z(t)$. Thus, it is referred to as the depth-independent matrix. Note that the components of $\boldsymbol{A}$ demonstrate a linear dependence on the

components of $\boldsymbol{M}$. When $\boldsymbol{M}$ is full rank, we hold the following properties [15]. It can be proven that the rank of matrix $\boldsymbol{A}$ is 2. For a homogeneous velocity vector $\sigma = (\sigma_1, \sigma_2, \sigma_3, 0)^T$, the fixed fourth entry of the third camera row contributes zero. The dependence on the 11 camera parameters can therefore be written as

$$\boldsymbol{A}(\boldsymbol{y}(t))\sigma = \boldsymbol{Q}(\sigma, \boldsymbol{y}(t))\boldsymbol{\vartheta}. \tag{2.11}$$

Here $\boldsymbol{Q}(\sigma, \boldsymbol{y}) \in \mathbb{R}^{3\times 11}$ is independent of the unknown camera parameters. The zero fourth component is satisfied by $\dot{\boldsymbol{x}} = \boldsymbol{J}\dot{\boldsymbol{q}}$.

2.2. The robotic dynamics model

The Lagrangian formulation is employed to present the dynamics equation of a robotic manipulator in the subsequent form:

$$\boldsymbol{H}(\boldsymbol{q}(t))\ddot{\boldsymbol{q}}(t) + (\frac{1}{2}\dot{\boldsymbol{H}}(\boldsymbol{q}(t)) + \boldsymbol{C}(\boldsymbol{q}(t), \dot{\boldsymbol{q}}(t)))\dot{\boldsymbol{q}}(t) + \boldsymbol{g}(\boldsymbol{q}(t)) = \boldsymbol{\tau}. \tag{2.12}$$

The first term in Eq (2.12) represents the forces due to the inertia of the robotic links, where $\boldsymbol{H}(\boldsymbol{q}(t)) \in \mathbb{R}_{n\times n}$ represents the positive-definite inertia matrix. The second term in the equation represents the forces due to the relative motion of the robotic links, including Coriolis and centrifugal effects, where $\boldsymbol{C}(\boldsymbol{q}(t), \dot{\boldsymbol{q}}(t))$ is a skew-symmetric matrix and has a property that, given an arbitrary vector, satisfies

$$\boldsymbol{a}^T\boldsymbol{C}(\boldsymbol{q}(t), \dot{\boldsymbol{q}}(t))\boldsymbol{a} = 0. \tag{2.13}$$

The symbol $\boldsymbol{g}(\boldsymbol{q}(t))$ is the gravity vector, which represents the gravitational forces acting on the robot. $\boldsymbol{\tau} \in \mathbb{R}_{n\times 1}$ is the vector of external torques applied to the robotic joints, including control torques and external forces.

Considering the asymmetric actuator backlash effect in robot joints, the practical actuator output can be described as

$$\tau(t) = B(v(t)), \tag{2.14}$$

where $v(t)$ is the backlash input and $B(v(t))$ represents the asymmetric actuator backlash constraint. In the practical environment, the presence of asymmetric actuator backlash is a common phenomenon. To describe its characteristics, the mathematics model is given as

$$\tau(t) = B(v(t)) = \begin{cases} m_r(v - B_r), \text{if } \dot{v} > 0 \text{ and } \tau(t) = m_r(v(t) - B_r), \\ m_l(v - B_l), \text{if } \dot{v} < 0 \text{ and } \tau(t) = m_l(v(t) - B_l), \\ \tau(t_-), \qquad\qquad \text{otherwise}, \end{cases} \tag{2.15}$$

where m_l and m_r denote the slopes of both sides, respectively, and the negative constant B_l and the positive constant B_r collectively constitute the width of the asymmetric actuator backlash. All four parameters are unknown. The notation $\tau(t_-)$ denotes the previously attained actuator output retained during a holding phase. An increasing input engages the right branch $m_r(v - B_r)$, and a decreasing input engages the left branch $m_l(v - B_l)$, once the corresponding boundary is reached. With positive slopes, $\text{sign}(\dot{v}) = \text{sign}(\dot{\tau})$ on an active branch. This convention is used by the branch indicators in Proposition 1

and the smooth inverse model. The state update uses the previous actuator output as its memory state. Let $\tau_r[k] = m_r(v[k] - B_r)$ and $\tau_l[k] = m_l(v[k] - B_l)$. After actuator initialization, the output is updated as

$$\tau[k] = \begin{cases} \tau_r[k], & \text{if } \dot{v}[k] > 0 \text{ and } \tau_r[k] \geq \tau[k-1], \\ \tau_l[k], & \text{if } \dot{v}[k] < 0 \text{ and } \tau_l[k] \leq \tau[k-1], \\ \tau[k-1], & \text{otherwise,} \end{cases}$$

where $\tau[k-1]$ is the stored actuator output. In the discrete implementation, the direction of $\dot{v}[k]$ is evaluated from $v[k] - v[k-1]$. The current branch value is compared with the stored output, and the stored output is retained until the active branch condition is met. The initialization used for the reported simulations is specified in Section 5.1.

The smooth inverse defined below uses tanh weighting functions, giving $X_r = X_l = 1/2$ when the torque-command rate is zero. This is compatible with the backlash memory: The actuator output retains its stored value whenever the actuator input remains within the gap associated with that output.

2.3. Smooth asymmetric backlash inverse

For unequal positive slopes, the two affine backlash branches intersect at a finite input value. Let N denote the absolute value of this intersection's input coordinate. The following assumption restricts the analysis to an interval in which the branches retain their specified order.

Assumption 1. *The actuator input satisfies $|v(t)| \leq N$ throughout the motion.*

Remark 1. Assumption 1 specifies the operating range of the asymmetric backlash model. Within this interval, the left branch remains on or above the right branch. The branch intersection defines the input bound used in the residual analysis.

Directly handling the non-smooth and multi-valued properties of the backlash model in (2.15) introduces significant difficulties for controller design and stability analysis, especially for gradient-based adaptive laws and Lyapunov-based proofs. Therefore, to construct a compensator that is both analytically tractable and effective, we employ a smooth inverse model to approximate the asymmetric backlash. The form of the inverse model is given as

$$v = BI(\tau_s) = (\tfrac{1}{m_r}\tau_s + B_r)X_r(\dot{\tau}_s) + (\tfrac{1}{m_l}\tau_s + B_l)X_l(\dot{\tau}_s), \tag{2.16}$$

where τ_s is the inverse model input and $\dot{\tau}_s$ is its rate, which selects the branch that the inverse has to reproduce, and $X_l(\dot{\tau}_s)$ and $X_r(\dot{\tau}_s)$ represent positive customizable functions, which are designed as

$$X_r(\dot{\tau}_s) = \frac{1 + \tanh(\kappa\dot{\tau}_s)}{2}, \tag{2.17}$$

$$X_l(\dot{\tau}_s) = \frac{1 - \tanh(\kappa\dot{\tau}_s)}{2}, \tag{2.18}$$

where κ is a positive adjustable parameter. For a fixed nonzero rate, increasing κ makes the weights approach the corresponding branch selector. The compensation residual is retained in the subsequent analysis. The following methodology is proposed for error handling between the smooth inverse and the dynamics asymmetric backlash.

Remark 2. The tanh weights provide a differentiable interpolation between the two inverse branches. The actuator hysteresis and its output-memory residual remain part of the model. The subsequent adaptive and robust terms account for the resulting compensation errors in the stability analysis.

Remark 3. The weighting functions satisfy $0 < X_r, X_l < 1$, and $X_r + X_l = 1$, and the parameter κ sets the steepness of the smooth transition between the inverse branches.

The inverse depends on unknown backlash parameters, which are estimated through an adaptive update law. Note that the parameters in the inverse model are coupled, which complicates direct parameter estimation. To facilitate the controller design and enhance its practical applicability, we make the following assumption:

Assumption 2. *The positive slope ratio $r = m_r/m_l$ is known and constant. The absolute slopes and backlash offsets remain unknown.*

This assumption enables a re-parameterization of the inverse model, thereby paving the way for the subsequent adaptive law design.

Hence, the relationship between m_r and m_l is fixed. Thus, the reparameterization of the smooth inverse model is possible. For simplicity, denote a constant by $m = m_r$ and the smooth inverse input τ_s can be written as

$$\tau_s = \boldsymbol{\varpi}^T \boldsymbol{\psi}_s(t), \tag{2.19}$$

where ϖ is the backlash parameter vector and $\psi_s(t)$ is the input-output dependent vector. Their form is as follows:

$$\boldsymbol{\varpi} = (m, -mB_r, -mB_l)^T \tag{2.20}$$

$$\boldsymbol{\psi}_s(t) = \frac{1}{X_r(\dot{\tau}_s) + rX_l(\dot{\tau}_s)}(v, X_r(\dot{\tau}_s), X_l(\dot{\tau}_s))^T. \tag{2.21}$$

Since the components of the vector ϖ are unknown, an update law is utilized to estimate them. The estimation process can be expressed as:

$$\hat{\boldsymbol{\varpi}} = (\hat{m}, -\widehat{mB_r}, -\widehat{mB_l})^T. \tag{2.22}$$

Then, the joint torque with the compensation of the inverse model is designed as follows:

$$\tau_d = \hat{\boldsymbol{\varpi}}^T \boldsymbol{\psi}_d(t). \tag{2.23}$$

Here τ_d is the torque command issued by the controller and $\dot{\tau}_d$ is its rate; the regressor $\boldsymbol{\psi}_d(t)$ is obtained from $\boldsymbol{\psi}_s(t)$ by replacing the rate of the inverse input $\dot{\tau}_s$ with the rate of the command $\dot{\tau}_d$. The signal τ_s is the input to the ideal inverse, whereas τ_d is the desired torque issued by the controller. Their regressors use $\dot{\tau}_s$ and $\dot{\tau}_d$, respectively. For the fixed regressor $\boldsymbol{\psi}_d$, replacing $\hat{\boldsymbol{\varpi}}$ by $\boldsymbol{\varpi}$ changes the represented torque by $\tilde{\boldsymbol{\varpi}}^T \boldsymbol{\psi}_d$. The actual actuator output additionally contains the backlash residual, as retained in (2.24); equality of the parameters alone does not remove the output-memory residual.

We define the notation $\widetilde{(\bullet)} = (\bullet) - \widehat{(\bullet)}$. Subsequently, the compensation error is derived as

$$\tau - \tau_d = \tilde{\varpi}^T \psi_d(t) + e(t), \tag{2.24}$$

where $\tilde{\varpi}^T \psi_d(t)$ is called the linearly parameterizable error, the form of the parameter error vector is $\tilde{\varpi} = (\widetilde{m}, \widetilde{-mB_r}, \widetilde{-mB_l})^T$, and $e(t) = \tau - \varpi^T \psi_d$ is the unparameterizable error term. For error $e(t)$, we have the following proposition:

Proposition 1. *When the adjustable parameter κ is sufficiently large in the smooth inverse model, the unparameterizable model error $e(t)$ remains bounded. The upper bound $\bar{D}$ satisfies the following condition:*

$$|e(t)| \leq \bar{D}. \tag{2.25}$$

Proof. $\tau = B(v(t))$ in (2.15) can be rewritten as

$$B(v) = m_r(v - B_r)\delta_r(\dot{\tau}) + m_l(v - B_l)\delta_l(\dot{\tau}) + \delta_z(\dot{\tau})\tau_z, \tag{2.26}$$

where $\delta_r(\dot{\tau})$, $\delta_l(\dot{\tau})$, $\delta_z(\dot{\tau})$ are the switch functions of the actuator-output rate $\dot{\tau}$, which are defined as:

$$\delta_r(\dot{\tau}) = \begin{cases} 1, & \text{if} \quad \dot{\tau} > 0, \\ 0, & \text{otherwise}, \end{cases} \tag{2.27}$$

$$\delta_l(\dot{\tau}) = \begin{cases} 1, & \text{if} \quad \dot{\tau} < 0, \\ 0, & \text{otherwise}, \end{cases} \tag{2.28}$$

$$\delta_z(\dot{\tau}) = \begin{cases} 1, & \text{if} \quad \dot{\tau} = 0, \\ 0, & \text{otherwise}. \end{cases} \tag{2.29}$$

In addition, by introducing the sign function sign(•), the slope rate r is rewritten as

$$r = \frac{\text{sign}(r-1)B_l - N}{\text{sign}(r-1)B_r - N}. \tag{2.30}$$

Case 1: If $\dot{\tau} > 0$, $\delta_r(\dot{\tau}) = 1$ and $\delta_l(\dot{\tau}) = \delta_z(\dot{\tau}) = 0$. $e(t)$ is given as

$$\begin{aligned} e(t) &= \tau - \varpi^T \psi_d \\ &= m_r(v - B_r) - \varpi^T \psi_d \\ &= (1 - \frac{1}{X_r(\dot{\tau}_d) + rX_l(\dot{\tau}_d)})mv \\ &\quad + \frac{X_l(\dot{\tau}_d)}{X_r(\dot{\tau}_d) + rX_l(\dot{\tau}_d)} mB_l + (\frac{X_r(\dot{\tau}_d)}{X_r(\dot{\tau}_d) + rX_l(\dot{\tau}_d)} - 1)mB_r. \end{aligned} \tag{2.31}$$

Denote the second and third terms by B_1. It can be obtained that when the variable κ is sufficiently large, B_1 has an upper and lower bound and

$$\frac{1}{X_r(\dot{\tau}_d) + rX_l(\dot{\tau}_d)} = \begin{cases} 1 + \varepsilon_1(t), & \text{if} \quad \dot{\tau}_d > 0, \\ \frac{1}{r} + \varepsilon_2(t), & \text{if} \quad \dot{\tau}_d < 0, \\ 2/(r+1), & \text{if} \quad \dot{\tau}_d = 0, \end{cases} \tag{2.32}$$

where $\varepsilon_1(t)$ and $\varepsilon_2(t)$ are infinitesimal as κ increases. The upper bound of B_1 is denoted by $\overline{B_1}$. The demonstration of the boundedness of the first term is as follows:

1) When $\dot{\tau}_d > 0$, by invoking $|v| \leq N$ in *Assumption 1*, (2.31), and (2.32), we obtain

$$|e(t)| \leq |\varepsilon_1 mN| + \bar{B}_1. \tag{2.33}$$

2) When $\dot{\tau}_d < 0$, the relationship of the error is given as

$$\begin{aligned} |e(t)| &\leq \left|(1 - \frac{1}{r} - \varepsilon_2)mN\right| + \bar{B}_1 \\ &\leq \left|\frac{(B_r - B_l)mN}{N - \text{sgn}(r-1)B_l}\right| + |\varepsilon_2 mN| + \bar{B}_1. \end{aligned} \tag{2.34}$$

3) When $\dot{\tau}_d = 0$, it can be written as

$$\begin{aligned} |e(t)| &\leq \left|(1 - \frac{2}{r+1})mN\right| + \bar{B}_1 \\ &\leq \left|\frac{(B_r - B_l)mN}{2N - \text{sgn}(r-1)(B_l + B_r)}\right| + \bar{B}_1. \end{aligned} \tag{2.35}$$

Hence, the boundedness of $e(t)$ is proved when $\dot{\tau} > 0$.

Case 2: If $\dot{\tau} < 0$, $\delta_l(\dot{\tau}) = 1$ and $\delta_r(\dot{\tau}) = \delta_z(\dot{\tau}) = 0$, by following the derivation of Case 1, the boundedness of $e(t)$ can be proven in the same way.

Case 3: If $\dot{\tau} = 0$, $\delta_z(\dot{\tau}) = 1$ and $\delta_r(\dot{\tau}) = \delta_l(\dot{\tau}) = 0$,

$$\begin{aligned} e(t) = (\tau_z(t) - \frac{mv}{X_r(\dot{\tau}_d) + rX_l(\dot{\tau}_d)}) \\ + \frac{X_l(\dot{\tau}_d)}{X_r(\dot{\tau}_d) + rX_l(\dot{\tau}_d)}mB_l + \frac{X_r(\dot{\tau}_d)}{X_r(\dot{\tau}_d) + rX_l(\dot{\tau}_d)}mB_r. \end{aligned} \tag{2.36}$$

Denote the second and third terms as

$$B_0 = \frac{X_l(\dot{\tau}_d)}{X_r(\dot{\tau}_d) + rX_l(\dot{\tau}_d)}mB_l + \frac{X_r(\dot{\tau}_d)}{X_r(\dot{\tau}_d) + rX_l(\dot{\tau}_d)}mB_r. \tag{2.37}$$

When κ is sufficiently large, B_0 is bounded.

1) When $\dot{\tau}_d > 0$, combining (2.31) and (2.32), we can obtain that

$$\begin{aligned} |e(t)| &\leq |\tau_z - (1 + \varepsilon_1)mv| + \bar{B}_0 \\ &\leq |\tau_z - mv| + |\varepsilon_1 mv| + \bar{B}_0. \end{aligned} \tag{2.38}$$

Due to the relationship $m_r(v - B_r) < \tau_z < m_l(v - B_l)$, and combining (2.30), we can obtain

$$\begin{aligned} |e(t)| \leq \max\left\{|mB_r|, \left|\frac{(B_r - B_l)mN}{N - \text{sgn}(r-1)B_l}\right| + \frac{|mB_l|}{r}\right\} \\ + |\varepsilon_1 mv| + \bar{B}_0. \end{aligned} \tag{2.39}$$

2) When $\dot{\tau}_d < 0$, we can similarly obtain

$$\begin{aligned} |e(t)| \leq \max\left\{\frac{1}{r}|mB_l|, \left|\frac{(B_r - B_l)mN}{N - \text{sgn}(r-1)B_l}\right| + |mB_r|\right\} \\ + |\varepsilon_2 mv| + \bar{B}_0. \end{aligned} \tag{2.40}$$

3) When $\dot{\tau}_d = 0$, we obtain

$$|e(t)| \leq \max\left\{|mB_r|, \frac{1}{r}|mB_l|\right\} + \bar{B}_0 + \left|\frac{(B_r - B_l)mN}{N - \text{sgn}(r-1)B_l}\right|. \tag{2.41}$$

The proof of the boundedness of $e(t)$ is established under the condition that $\dot{\tau} = 0$.

□

Thus, taking into account the backlash effect, the manipulator dynamics equation is expressed as

$$\begin{aligned} &\boldsymbol{H}(\boldsymbol{q}(t))\ddot{\boldsymbol{q}}(t) + (\frac{1}{2}\dot{\boldsymbol{H}}(\boldsymbol{q}(t)) + \boldsymbol{C}(\boldsymbol{q}(t), \dot{\boldsymbol{q}}(t))\dot{\boldsymbol{q}}(t) + \boldsymbol{g}(\boldsymbol{q}(t)) \\ &= \boldsymbol{\tau}_d + \tilde{\boldsymbol{\varsigma}}^T\boldsymbol{\Psi} + \boldsymbol{E}. \end{aligned} \tag{2.42}$$

The ith entry of $\tilde{\boldsymbol{\varsigma}}^T\boldsymbol{\Psi}$ is $\tilde{\boldsymbol{\varpi}}_i^T\boldsymbol{\psi}_i$, where $\boldsymbol{\psi}_i = \boldsymbol{\psi}_{d,i}$. Equivalently, $\tilde{\boldsymbol{\varsigma}} = \text{diag}(\tilde{\boldsymbol{\varpi}}_1, \ldots, \tilde{\boldsymbol{\varpi}}_n) \in \mathbb{R}^{3n\times n}$ and $\boldsymbol{\Psi} = (\boldsymbol{\psi}_1^T, \ldots, \boldsymbol{\psi}_n^T)^T \in \mathbb{R}^{3n}$. The vector $\boldsymbol{E} = (e_1, \ldots, e_n)^T$ contains the nonparameterizable residuals.

3. Controller design

The controller combines camera-parameter estimation, an adaptive backlash inverse, and robust compensation. The camera estimate, backlash parameter estimates, and robust gains are updated concurrently from the signals specified below. The convergence conditions are stated in Section 4.

3.1. Visual controller

Denote the constant vector $\boldsymbol{y}_d$ as the desired image coordinates. Thus, the visual feedback image error is as follows:

$$\Delta\boldsymbol{y}(t) = \boldsymbol{y}(t) - \boldsymbol{y}_d. \tag{3.1}$$

Note that the third row of $\Delta\boldsymbol{y}(t)$ is zero. Since $\boldsymbol{y}_d$ is constant and one feature point is used, the task is *single-point image-space setpoint regulation*. A single feature point provides two image constraints. Under pinhole projection, different admissible depths along the same projection ray give the same image point. The image target alone therefore does not specify a unique three-dimensional position or pose of the end effector. For the three-joint model in Section 5, when the two image constraints are independent, one local direction of joint motion remains unspecified by the image task. The final joint configuration is thus not prescribed by the image target alone. Through the feedback on joint angles, velocities, and image error, utilizing the estimated camera parameters $\hat{\boldsymbol{\vartheta}}$, the designed controller $\boldsymbol{\tau}_d$ is given as:

$$\boldsymbol{\tau}_d = \boldsymbol{g}(\boldsymbol{q}) - \boldsymbol{K}_1\dot{\boldsymbol{q}}(t) - \boldsymbol{J}^T(\boldsymbol{q}(t))[\hat{\boldsymbol{A}}^T(\boldsymbol{y}(t)) + \frac{1}{2}\hat{\boldsymbol{m}}_3(t)\Delta\boldsymbol{y}^T(t)]\boldsymbol{B}\Delta\boldsymbol{y}(t) + \boldsymbol{\tau}_{\boldsymbol{0}}. \tag{3.2}$$

The first term is designed to eliminate the effects of gravity in the robot dynamics. The third term introduces the image error $\Delta\boldsymbol{y}(t)$. Here, $\hat{\boldsymbol{A}}(\boldsymbol{y}(t))$ and $\hat{\boldsymbol{M}}$ estimate $\boldsymbol{A}(\boldsymbol{y}(t))$ and $\boldsymbol{M}$, respectively, and

$\hat{\boldsymbol{m}}_3^T(t)$ is the third row of $\hat{\boldsymbol{M}}$. $\boldsymbol{K}_1 \in \mathbb{R}_{n\times n}$ is the positive velocity gain matrix. $\boldsymbol{B} \in \mathbb{R}_{3\times 3}$ is the position gain matrix, taken throughout as $\boldsymbol{B} = \text{diag}(b_1, b_2, b_3)$ with $b_i > 0$. The term $\boldsymbol{\tau_0}$ is the adaptive robust compensator designed to compensate for the unparameterizable errors $\boldsymbol{E}$. The proposed compensator structure is as follows:

$$\boldsymbol{\tau_0} = -\hat{\boldsymbol{D}}\,\text{sign}(\dot{\boldsymbol{q}}(t)), \tag{3.3}$$

where $\hat{\boldsymbol{D}}$ is the estimation of $\boldsymbol{D}$ and the matrix $\boldsymbol{D}$ is a diagonal matrix with elements D_n. It is constructed as

$$\boldsymbol{D} = diag(D_1, D_2, ..., D_n), \tag{3.4}$$

where D_n represent the upper limit of the unparameterizable error $|e_n|$.

Remark 4. The discontinuous robust term can cause chattering in a sampled or bandwidth-limited implementation. Section 4 analyzes the nominal sign law. Continuous alternatives include $\text{sat}(\dot{q}_i/\varepsilon)$ and $\tanh(\kappa_0\dot{q}_i)$, with $\varepsilon, \kappa_0 > 0$. Their deviations from the sign law satisfy

$$0 \le |x| - x\,\text{sat}(x/\varepsilon) \le \varepsilon/4, \qquad 0 \le |x| - x\tanh(\kappa_0 x) \le 0.2785/\kappa_0. \tag{3.5}$$

These inequalities quantify additional terms in the Lyapunov estimate when the robust command is smoothed. They do not alone establish an ultimate bound for the full state or convergence of the image error. A smoothed implementation requires a separate stability argument; Theorem 1 concerns the stated sign law and adaptive updates. In practical application, the sign term may also be replaced by a saturation function; such a continuous alternative provides a trade-off between asymptotic stability and control performance. □

By introducing the controller (3.2) into the modified dynamics equation considering the backlash effect in (2.42), the dynamic equation under the action of the controller is as follows:

$$\begin{aligned}
&\boldsymbol{H}(\boldsymbol{q}(t))\ddot{\boldsymbol{q}}(t) + \left(\frac{1}{2}\dot{\boldsymbol{H}}(\boldsymbol{q}(t)) + \boldsymbol{C}(\boldsymbol{q}(t), \dot{\boldsymbol{q}}(t))\right)\dot{\boldsymbol{q}}(t) \\
&= -\boldsymbol{K}_1\dot{\boldsymbol{q}}(t) - \boldsymbol{J}^T(\boldsymbol{q}(t))\left[\boldsymbol{A}^T(\boldsymbol{y}(t)) + \frac{1}{2}\boldsymbol{m}_3\Delta\boldsymbol{y}^T(t)\right]\boldsymbol{B}\Delta\boldsymbol{y}(t) \\
&- \boldsymbol{J}^T(\boldsymbol{q}(t))[\hat{\boldsymbol{A}}^T(\boldsymbol{y}(t)) - \boldsymbol{A}^T(\boldsymbol{y}(t)) + \frac{1}{2}\hat{\boldsymbol{m}}_3(t)\Delta\boldsymbol{y}^T(t) - \frac{1}{2}\boldsymbol{m}_3\Delta\boldsymbol{y}^T(t)]\boldsymbol{B}\Delta\boldsymbol{y}(t) \\
&+ \widetilde{\boldsymbol{\varsigma}}^T\boldsymbol{\Psi} + \boldsymbol{E} + \boldsymbol{\tau_0}.
\end{aligned} \tag{3.6}$$

Using the linear dependence on the parameter error in the term containing the estimate $\hat{\boldsymbol{\vartheta}}$, it is feasible to isolate the unknown parameters. Consequently, this term can be reformulated as

$$\begin{aligned}
&- \boldsymbol{J}^T(\boldsymbol{q}(t))[\hat{\boldsymbol{A}}^T(\boldsymbol{y}(t)) - \boldsymbol{A}^T(\boldsymbol{y}(t)) \\
&+ \frac{1}{2}\hat{\boldsymbol{m}}_3(t)\Delta\boldsymbol{y}^T - \frac{1}{2}\boldsymbol{m}_3\Delta\boldsymbol{y}^T]\boldsymbol{B}\Delta\boldsymbol{y}(t) \\
&= \boldsymbol{Y}(\boldsymbol{q}(t), \boldsymbol{y}(t))\Delta\boldsymbol{\vartheta}(t),
\end{aligned} \tag{3.7}$$

where the matrix $\boldsymbol{Y}(\boldsymbol{q}(t), \boldsymbol{y}(t))$ is independent of the unknown parameters and $\Delta\boldsymbol{\vartheta} = \hat{\boldsymbol{\vartheta}} - \boldsymbol{\vartheta}$ is the camera-parameter estimation error.

3.2. Adaptive rule

In this paper, three adaptive update rules are proposed for updating the estimation of the unknown camera and asymmetric backlash parameter, and for compensating unparameterized errors, respectively. The construction method of the first adaptive law is given as follows:

It is assumed that at a time instant t_j, the homogeneous coordinate of the feature point is $\boldsymbol{x}(t_j)$ and the projection coordinate is $\boldsymbol{y}(t_j)$. The estimation projection error at the stored position is defined as

$$\begin{aligned} e_c(t_j, t) &= \boldsymbol{y}(t_j)(\hat{\boldsymbol{m}}_3^T - \boldsymbol{m}_3^T)\boldsymbol{x}(t_j) - (\hat{\boldsymbol{M}} - \boldsymbol{M})\boldsymbol{x}(t_j) \\ &= \boldsymbol{W}(\boldsymbol{x}(t_j), \boldsymbol{y}(t_j))\Delta\boldsymbol{\vartheta}. \end{aligned} \tag{3.8}$$

Here, m points can be selected to generate m equations similar to Eq (3.8) along the trajectory of the feature point. Once the base coordinate of the feature points is fixed, the regression matrix $\boldsymbol{W}(t_j)$ becomes a known matrix. The adaptive update law for $\hat{\boldsymbol{\vartheta}}$ is designed as:

$$\dot{\hat{\boldsymbol{\vartheta}}} = -\boldsymbol{\Gamma}^{-1}\left\{\boldsymbol{Y}^T\dot{\boldsymbol{q}} + \sum_{j=1}^{m}\boldsymbol{W}(t_j)^T\boldsymbol{K}_3\boldsymbol{e}_c(t_j, t)\right\}. \tag{3.9}$$

Here $\boldsymbol{\Gamma} \in \mathbb{R}^{11\times11}$ and $\boldsymbol{K}_3 \in \mathbb{R}^{3\times3}$ are positive-definite gain matrices, and $\boldsymbol{W}(t_j) \in \mathbb{R}^{3\times11}$.

Remark 5. The selection of the m positions is the guarantee of convergence of the adaptive camera parameters. To ensure parameter convergence, a sufficient condition is that at least five points are chosen such that no three of their image projections are collinear. The two terms of (3.9) play different roles, and it is worth separating them because the two terms of the final bound (4.8) are a different pair. The first term of (3.9) is what allows the Lyapunov derivative to be non-positive at all. The camera-parameter estimation error enters the closed-loop dynamics through the parameterization, and premultiplying the dynamics by $\dot{\boldsymbol{q}}^T(t)$ produces the sign-indefinite contribution $+\dot{\boldsymbol{q}}^T(t)\boldsymbol{Y}(\boldsymbol{q}(t), \boldsymbol{y}(t))\Delta\boldsymbol{\vartheta}$; premultiplying (3.9) by $\Delta\boldsymbol{\vartheta}^T\boldsymbol{\Gamma}$ produces exactly its negative, and the two cancel. The second term does not cancel anything: it generates a negative semi-definite term of its own, namely, $-\sum_{j=1}^{m}\Delta\boldsymbol{\vartheta}^T\boldsymbol{W}(t_j)\boldsymbol{K}_3\boldsymbol{W}(t_j)^T\Delta\boldsymbol{\vartheta}$, which is the second term of (4.8), so that $\boldsymbol{W}(t_j)\Delta\boldsymbol{\vartheta} \to 0$ in Section 4; the selection condition is what makes this limit imply $\operatorname{rank}(\hat{\boldsymbol{M}}) = 3$, the property on which the stability argument rests. Indeed, if $\operatorname{rank}(\hat{\boldsymbol{M}}) < 3$ then $c_1\hat{\boldsymbol{m}}_1^T + c_2\hat{\boldsymbol{m}}_2^T + c_3\hat{\boldsymbol{m}}_3^T = \boldsymbol{0}$ for some c_1, c_2, c_3 not all zero, and substituting this into $e_c(t_j, t) = \boldsymbol{0}$ with $\boldsymbol{y}(t_j) = (u_j, v_j, 1)^T$ gives

$$u_jc_1 + v_jc_2 + c_3 = 0, \tag{3.10}$$

i.e., the projection (u_j, v_j) lies on the line $c_1u + c_2v + c_3 = 0$. Hence a nonzero (c_1, c_2, c_3) can satisfy (3.10) at every recorded instant only if all the recorded projections lie on one and the same line. Recording projections among which three are not collinear therefore excludes any nonzero (c_1, c_2, c_3), and $\operatorname{rank}(\hat{\boldsymbol{M}}) = 3$; this is Proposition 2 of [15]. □

In practice, one records the base and image coordinates during motion and selects samples after checking the non-collinearity of their image projections. This procedure does not prescribe a particular trajectory or impose an additional initial-configuration constraint beyond the stated operating domain. To reduce the backlash effect, the corresponding adaptive rule to update the parameter estimations of the smooth inverse model is designed as

$$\dot{\hat{\boldsymbol{\varpi}}}_i = \boldsymbol{\Upsilon}_i^{-1}\boldsymbol{\psi}_i\dot{q}_i(t), \tag{3.11}$$

where Υ_i is the diagonal gain matrix. This adaptive rule is utilized to estimate the actuator parameters of different joints. The sign is fixed by the stability argument: since $\dot{\tilde{\boldsymbol{\varpi}}}_i = -\dot{\hat{\boldsymbol{\varpi}}}_i$, rule (3.11) contributes $-\tilde{\boldsymbol{\varpi}}_i^T \boldsymbol{\psi}_i \dot{q}_i(t)$ to the Lyapunov derivative, which is exactly what is needed to cancel the parameterized compensation error $\tilde{\boldsymbol{\varpi}}_i^T \boldsymbol{\psi}_i \dot{q}_i(t)$ produced by the term $\tilde{\boldsymbol{\varsigma}}^T \boldsymbol{\Psi}$ of (2.42); see Section 4.

Furthermore, to approximate the upper bound of the unparameterizable error of the asymmetric backlash inverse model, the adaptive rule designed for the backlash constraint compensator is given as

$$\dot{\hat{D}}_i = \xi_i^{-1} |\dot{q}_i|, \qquad i = 1, \ldots, n. \tag{3.12}$$

Here $\boldsymbol{\Xi} = \mathrm{diag}(\xi_1, \ldots, \xi_n) \succ 0$ and $\hat{\boldsymbol{D}} = \mathrm{diag}(\hat{D}_1, \ldots, \hat{D}_n)$.

Extension to multiple feature points. We follow the extension to several feature points given in Section IV of [15]. Let S denote the number of feature points. The image errors of all points are stacked into one error vector $\Delta \boldsymbol{y}$ with $2S$ independent components, and the depth-independent interaction matrices of the individual points are stacked correspondingly. The controller of [15, Eq (39)] keeps the same structure, with the single-point error and interaction matrix replaced by their stacked counterparts; it is noted there that the Jacobian differs from point to point. The camera-parameter update keeps its structure as well [15, Eq (42)], applied to a set of recorded spatial positions of each point together with the corresponding projections, the number of recorded positions per point being chosen large enough for the associated rank condition to hold. All points must remain visible with depths bounded away from zero throughout the admissible motion.

With this stacking, the stability argument is unchanged up to the equilibrium condition, which becomes $\hat{\boldsymbol{J}}^T \boldsymbol{K}_2 \Delta \boldsymbol{y} = \boldsymbol{0}$ [15, Eq (43)]. As in the single-point case, convergence of the image errors to zero does not follow from that condition alone. [15] states that the image errors converge to zero only when the rank of the coefficient matrix in that condition is equal to $2S$. This implies that the number n of DOFs of the manipulator must be larger than or equal to $2S$. For the single-point case treated in this paper, $S = 1$ and $2S = 2 \leq n = 3$, so the rank condition can be met and one joint direction is left unconstrained by the image error—exactly the free direction discussed above. Driving the image error of every point to zero with no unconstrained direction would require $n \geq 2S$; a six-degree-of-freedom pose-regulation task calls for $S \geq 3$ points together with $n \geq 6$. When all points are rigidly attached to the end effector, [15] obtains a stronger statement: The equilibrium condition reduces to $2S$ nonlinear equations in the six unknowns of the end-effector pose, three translational and three rotational, and the image errors converge to zero only if that system admits the desired pose as its unique solution; if it admits more than one solution, convergence to zero is not guaranteed, and the conditions for uniqueness are left open there. This extension is identified as a direction for future work.

4. Stability analysis

The projection conditions used in the stability analysis are stated below.

Assumption 3. *There exists a constant $z_{\min} > 0$ such that the feature depth satisfies ${}^c z(\boldsymbol{q}(t)) \geq z_{\min}$. The forward-kinematic map is continuously differentiable on the operating domain.*

Assumption 4. *For the independent image coordinates u and v, define*

$$\boldsymbol{J}_v(\boldsymbol{q}) = \frac{1}{{}^c z(\boldsymbol{q})} \boldsymbol{A}_{uv}(\boldsymbol{y}) \boldsymbol{J}(\boldsymbol{q}) \in \mathbb{R}^{2 \times n},$$

where $\boldsymbol{A}_{uv}(\boldsymbol{y}) \in \mathbb{R}^{2\times 4}$ consists of the first two rows of $\boldsymbol{A}(\boldsymbol{y})$, so that $(\dot{u}, \dot{v})^T = \boldsymbol{J}_v \dot{\boldsymbol{q}}$. On the operating domain, there exists a constant $\underline{\sigma} > 0$ such that $\sigma_{\min}(\boldsymbol{J}_v) \geq \underline{\sigma}$, ensuring a full row rank of two.

The operating domain comprises the joint configurations satisfying Assumptions 3 and 4 for which the feature lies within the image window. The image-task rank condition is imposed on $\boldsymbol{J}_v$; the analysis does not require inversion of the full manipulator Jacobian. The additional rank condition for zero limiting image error is stated separately in Theorem 1.

The analysis concerns complete closed-loop solutions on the operating domain above, for which the inverse model is well-defined. The mechanical and adaptive states are absolutely continuous, and their equations hold almost everywhere. We use the standard regularity of the rigid-manipulator model: $\boldsymbol{H}(\boldsymbol{q}) \geq h_0 \boldsymbol{I}_n$ for some $h_0 > 0$, and the model functions and derivatives of $\boldsymbol{H}$ are bounded on bounded configuration and velocity sets. All initial states are finite. The recorded data are fixed after a finite time t_0, so that $\boldsymbol{W}_j := \boldsymbol{W}(t_j)$ is constant for $t \geq t_0$. All gain matrices are positive definite, and $\boldsymbol{\Xi} = \operatorname{diag}(\xi_1, \ldots, \xi_n)$ with $\xi_i > 0$. Proposition 1 supplies finite constants D_i satisfying $|e_i(t)| \leq D_i$.

To retain the actual compensation terms in the final balance, define

$$\hat{\boldsymbol{\Lambda}}(t) = \hat{\boldsymbol{A}}^T(\boldsymbol{y}(t)) + \tfrac{1}{2}\hat{\boldsymbol{m}}_3(t)\Delta\boldsymbol{y}^T(t), \tag{4.1}$$

$$\boldsymbol{R}(t) = \tilde{\boldsymbol{\zeta}}^T\boldsymbol{\Psi} + \boldsymbol{E} + \boldsymbol{\tau}_0 = \boldsymbol{\tau} - \boldsymbol{\tau}_d + \boldsymbol{\tau}_0. \tag{4.2}$$

Let $\boldsymbol{\eta} = (\Delta u, \Delta v)^T$, $\boldsymbol{B}_{uv} = \operatorname{diag}(b_1, b_2)$, and

$$\boldsymbol{P} = \begin{pmatrix} 1 & 0 \\ 0 & 1 \\ 0 & 0 \end{pmatrix}, \qquad \Delta\boldsymbol{y} = \boldsymbol{P}\boldsymbol{\eta}.$$

The matrix mapping the two independent image errors to the feedback torque is

$$\boldsymbol{\mathcal{G}}(t) = \boldsymbol{J}(\boldsymbol{q}(t))^T \hat{\boldsymbol{\Lambda}}(t)\boldsymbol{P}\boldsymbol{B}_{uv} \in \mathbb{R}^{n\times 2}. \tag{4.3}$$

This matrix includes the estimated camera parameters and is distinct from the true visual Jacobian in Assumption 4.

Theorem 1. *Consider a complete solution satisfying Assumptions 1–4 and the regularity conditions stated above, with controller (3.2) and adaptive laws (3.9)–(3.12). The joint configuration and velocity, image error, parameter estimates, robust gains, and torque signals remain bounded. Moreover,*

$$\dot{\boldsymbol{q}}(t) \to \boldsymbol{0}, \qquad \boldsymbol{W}_j\Delta\boldsymbol{\vartheta}(t) \to \boldsymbol{0},$$

and $\boldsymbol{q}$, $\Delta\boldsymbol{y}$, $\hat{\boldsymbol{\vartheta}}$, $\hat{\boldsymbol{\varpi}}_i$, and $\hat{D}_i$ have finite limits. Write the limiting two-dimensional image error as $\boldsymbol{\eta}_\infty$ and the limit of (4.3) as $\boldsymbol{\mathcal{G}}_\infty$.

If $\operatorname{rank}\boldsymbol{\mathcal{G}}_\infty = 2$ *and* $\limsup_{t\to\infty}\|\boldsymbol{R}(t)\| \leq \bar{R}$, *then*

$$\|\boldsymbol{\eta}_\infty\| \leq \frac{\bar{R}}{\sigma_{\min}(\boldsymbol{\mathcal{G}}_\infty)}. \tag{4.4}$$

In particular, if $\boldsymbol{R}(t) \to \boldsymbol{0}$, then $\Delta\boldsymbol{y}(t) \to \boldsymbol{0}$. The same zero-error conclusion holds if the average of $\boldsymbol{R}$ over a fixed positive time window tends to zero. The rank and net-residual conditions are additional conditions for zero image error; they are not consequences of the boundedness result alone.

Proof. Set $\Delta\boldsymbol{\vartheta} = \hat{\boldsymbol{\vartheta}} - \boldsymbol{\vartheta}$, $\tilde{\boldsymbol{\varpi}}_i = \boldsymbol{\varpi}_i - \hat{\boldsymbol{\varpi}}_i$, and $\tilde{D}_i = D_i - \hat{D}_i$. Use the Lyapunov function

$$V = \tfrac{1}{2}\left\{ {}^{c}z\,\Delta\boldsymbol{y}^T\boldsymbol{B}\Delta\boldsymbol{y} + \dot{\boldsymbol{q}}^T\boldsymbol{H}\dot{\boldsymbol{q}} + \Delta\boldsymbol{\vartheta}^T\boldsymbol{\Gamma}\Delta\boldsymbol{\vartheta} + \sum_{i=1}^{n}\left(\tilde{\boldsymbol{\varpi}}_i^T\boldsymbol{\Upsilon}_i\tilde{\boldsymbol{\varpi}}_i + \xi_i\tilde{D}_i^2\right)\right\}. \tag{4.5}$$

The corrected image-velocity identity and the derivative of the image-energy term are

$$\dot{\boldsymbol{q}}^T\boldsymbol{J}^T\boldsymbol{A}^T = {}^{c}z\,\Delta\dot{\boldsymbol{y}}^T, \tag{4.6}$$

$$\frac{d}{dt}\left(\tfrac{1}{2}{}^{c}z\,\Delta\boldsymbol{y}^T\boldsymbol{B}\Delta\boldsymbol{y}\right) = \dot{\boldsymbol{q}}^T\boldsymbol{J}^T\left(\boldsymbol{A}^T + \tfrac{1}{2}\boldsymbol{m}_3\Delta\boldsymbol{y}^T\right)\boldsymbol{B}\Delta\boldsymbol{y}. \tag{4.7}$$

Here $\Delta\dot{\boldsymbol{y}} = \dot{\boldsymbol{y}}$ because the image target is constant, and ${}^{c}\dot{z} = \boldsymbol{m}_3^T\boldsymbol{J}\dot{\boldsymbol{q}}$.

The camera parameter-error cross term cancels through (3.9), and the backlash parameter-error cross terms cancel through (3.11). The componentwise update (3.12) cancels the terms involving $\tilde{D}_i|\dot{q}_i|$. With $\boldsymbol{e}_{c,j} = \boldsymbol{W}_j\Delta\boldsymbol{\vartheta}$, differentiation therefore gives, almost everywhere,

$$\begin{aligned}\dot{V} &= -\dot{\boldsymbol{q}}^T\boldsymbol{K}_1\dot{\boldsymbol{q}} - \sum_j \boldsymbol{e}_{c,j}^T\boldsymbol{K}_3\boldsymbol{e}_{c,j} + \sum_i\left(\dot{q}_i e_i - D_i|\dot{q}_i|\right)\\ &\le -\dot{\boldsymbol{q}}^T\boldsymbol{K}_1\dot{\boldsymbol{q}} - \sum_j \boldsymbol{e}_{c,j}^T\boldsymbol{K}_3\boldsymbol{e}_{c,j} \le 0.\end{aligned} \tag{4.8}$$

The same inequality holds for the Filippov interpretation of the robust term: At a zero joint velocity, its product with any admissible value of that robust term is zero. No particular cancelling value is selected in this argument.

It follows that $0 \le V(t) \le V(t_0)$. The positive depth and inertia bounds give boundedness of $\Delta\boldsymbol{y}$ and $\dot{\boldsymbol{q}}$, while the positive parameter weights give boundedness of the estimation errors and estimates. In particular, each $\hat{D}_i$ is bounded and, by (3.12), nondecreasing. Hence they have finite limits and

$$\int_{t_0}^{\infty}|\dot{q}_i(t)|\,dt = \xi_i(\hat{D}_i(\infty) - \hat{D}_i(t_0)) < \infty. \tag{4.9}$$

Thus $\dot{\boldsymbol{q}} \in L_1$ and $\boldsymbol{q}(t)$ has a finite limit $\boldsymbol{q}_\infty$.

Assumption 1 and $X_r + rX_l \ge \min\{1, r\} > 0$ give bounded regressors $\boldsymbol{\psi}_i$. The parameterized torque error, $\boldsymbol{E}$, and $\boldsymbol{\tau}_0$ are therefore bounded. The controller and the compensation-error identity then give bounded commanded and actual actuator torques. On the bounded configuration and velocity set, the remaining model terms are bounded, and the inertia lower bound gives bounded $\ddot{\boldsymbol{q}}$ almost everywhere. Consequently, $\dot{\boldsymbol{q}}$ is uniformly continuous. Equation (3.9) also gives bounded $\dot{\hat{\boldsymbol{\vartheta}}}$, so each $\boldsymbol{e}_{c,j}$ is uniformly continuous.

Integrating (4.8) shows that $\dot{\boldsymbol{q}}^T\boldsymbol{K}_1\dot{\boldsymbol{q}}$ and each $\boldsymbol{e}_{c,j}^T\boldsymbol{K}_3\boldsymbol{e}_{c,j}$ belong to L_1. Their bounded signals and bounded derivatives make these quadratic quantities uniformly continuous. Barbalat's lemma then yields

$$\dot{\boldsymbol{q}}(t) \to \boldsymbol{0}, \qquad \boldsymbol{W}_j\Delta\boldsymbol{\vartheta}(t) \to \boldsymbol{0}. \tag{4.10}$$

The projection is continuous at $\boldsymbol{q}_\infty$ because its depth is bounded away from zero; hence $\Delta\boldsymbol{y}$ has a finite limit. Also, bounded $\boldsymbol{\psi}_i$ and (4.9) imply $\dot{\tilde{\boldsymbol{\varpi}}}_i \in L_1$, so every backlash parameter estimate has a finite limit.

For the camera parameter estimate, let

$$\boldsymbol{Q}_h = \sum_j \boldsymbol{W}_j^T \boldsymbol{K}_3 \boldsymbol{W}_j \geq 0.$$

The camera parameter error satisfies

$$\boldsymbol{\Gamma}\Delta\dot{\boldsymbol{\vartheta}} = -\boldsymbol{Q}_h\Delta\boldsymbol{\vartheta} - \boldsymbol{Y}^T\dot{\boldsymbol{q}}. \tag{4.11}$$

With $\boldsymbol{z}_\theta = \boldsymbol{\Gamma}^{1/2}\Delta\boldsymbol{\vartheta}$, this becomes

$$\dot{\boldsymbol{z}}_\theta = -\boldsymbol{L}_\theta\boldsymbol{z}_\theta + \boldsymbol{f}(t), \qquad \boldsymbol{L}_\theta = \boldsymbol{\Gamma}^{-1/2}\boldsymbol{Q}_h\boldsymbol{\Gamma}^{-1/2} \geq 0, \qquad \boldsymbol{f} = -\boldsymbol{\Gamma}^{-1/2}\boldsymbol{Y}^T\dot{\boldsymbol{q}} \in L_1.$$

In each positive-eigenvalue direction of the symmetric matrix $\boldsymbol{L}_\theta$, the exponentially decaying initial response and its convolution with the L_1 input tend to zero. In each zero-eigenvalue direction, the state is its initial value plus a convergent integral of that input. Thus $\hat{\boldsymbol{\vartheta}}$ has a finite limit, with $\boldsymbol{Q}_h\Delta\boldsymbol{\vartheta}_\infty = 0$. This algebraic condition is all that is asserted about the limiting estimates; no stronger property is inferred from it. Continuity then gives a finite limit $\boldsymbol{\mathcal{G}}_\infty$.

Using the estimated camera matrix directly in the controller gives the exact mechanical balance

$$\boldsymbol{H}\ddot{\boldsymbol{q}} + (\tfrac{1}{2}\dot{\boldsymbol{H}} + \boldsymbol{C})\dot{\boldsymbol{q}} = -\boldsymbol{K}_1\dot{\boldsymbol{q}} - \boldsymbol{\mathcal{G}}\boldsymbol{\eta} + \boldsymbol{R}. \tag{4.12}$$

The camera parameter-error term $\boldsymbol{Y}\Delta\boldsymbol{\vartheta}$ is not added again in this representation. The residual $\boldsymbol{R}$ retains the actual actuator output, including its backlash memory, and is bounded by the estimates and regressors already bounded above.

Fix $T > 0$. Integration of (4.12) gives

$$\begin{aligned}\frac{1}{T}\int_t^{t+T} \boldsymbol{R}(s)\,ds = \frac{[\boldsymbol{H}\dot{\boldsymbol{q}}]_t^{t+T}}{T} + \frac{1}{T}\int_t^{t+T} (\boldsymbol{C} - \tfrac{1}{2}\dot{\boldsymbol{H}} + \boldsymbol{K}_1)\dot{\boldsymbol{q}}\,ds \\ + \frac{1}{T}\int_t^{t+T} \boldsymbol{\mathcal{G}}(s)\boldsymbol{\eta}(s)\,ds.\end{aligned} \tag{4.13}$$

The first two terms tend to zero because $\dot{\boldsymbol{q}} \to 0$ and their coefficients are bounded. The last term tends to $\boldsymbol{\mathcal{G}}_\infty\boldsymbol{\eta}_\infty$. Hence

$$\lim_{t\to\infty} \frac{1}{T}\int_t^{t+T} \boldsymbol{R}(s)\,ds = \boldsymbol{\mathcal{G}}_\infty\boldsymbol{\eta}_\infty. \tag{4.14}$$

This step does not assume that $\ddot{\boldsymbol{q}}$ converges, or that the discontinuous robust term has a pointwise limit.

If $\limsup \|\boldsymbol{R}(t)\| \leq \bar{R}$, the norm of the limit in (4.14) is at most $\bar{R}$. When $\boldsymbol{\mathcal{G}}_\infty$ has full column rank,

$$\sigma_{\min}(\boldsymbol{\mathcal{G}}_\infty)\|\boldsymbol{\eta}_\infty\| \leq \|\boldsymbol{\mathcal{G}}_\infty\boldsymbol{\eta}_\infty\| \leq \bar{R},$$

which proves (4.4). If the net-residual average is zero, in particular if $\boldsymbol{R}(t) \to 0$, the same rank condition gives $\boldsymbol{\eta}_\infty = 0$ and therefore $\Delta\boldsymbol{y} \to 0$. □

The Lyapunov inequality controls the residual power along the joint velocity; it does not by itself imply $\boldsymbol{R} \to 0$. A stationary state must satisfy $\boldsymbol{\tau} = \boldsymbol{g}(\boldsymbol{q})$ and the backlash memory conditions, together with $\boldsymbol{\mathcal{G}}\boldsymbol{\eta} = \boldsymbol{R}$. A nonzero image error can therefore be balanced by a nonzero residual. Theorem 1 states zero image error only under the additional rank and net-residual conditions. The estimates are shown to be bounded with finite limits, and no stronger property is inferred for them. The convergence statement concerns image-space setpoint regulation and does not specify a unique three-dimensional end-effector pose. Conditions for a multi-feature formulation are discussed in Section 3.

5. Performance tests

The simulations use a three-joint manipulator model based on the PUMA 560 parameterization, with the D-H parameters listed in Table 1. The control architecture and the fixed-camera configuration are shown in Figures 2 and 3. Figures 4–13 present the nominal experiments with continuous visual feedback generated from the projection model. Sections 5.1–5.2 report supplementary tests of finite-rate visual feedback, camera estimation, and controller variants, with their settings stated separately.

The simulation retains the first three joints of this parameterization. In the PUMA 560, these joints position the wrist center in space, whereas the last three joints are wrist joints that adjust the end-effector orientation finely. Since the backlash compensation is applied joint by joint, the retained joints carry every mechanism under study, and omitting the wrist joints removes no part of it. The controller, the adaptive laws, and the Lyapunov function are stated for a general joint index and are not limited to three joints, so the formulation extends directly to manipulators with more actuated joints; the visual part continues to require the rank condition of Assumption 4 on the operating domain. The single-point task itself does not prescribe the full end-effector pose.

Table 1. D-H parameters of the manipulator.

Joint	Angle (rad)	Offset (m)	Length (m)	Twist (rad)
1	q_1	0	0	$\pi/2$
2	q_2	0	0.3318	0
3	q_3	0.15005	0.1285	$-\pi/2$

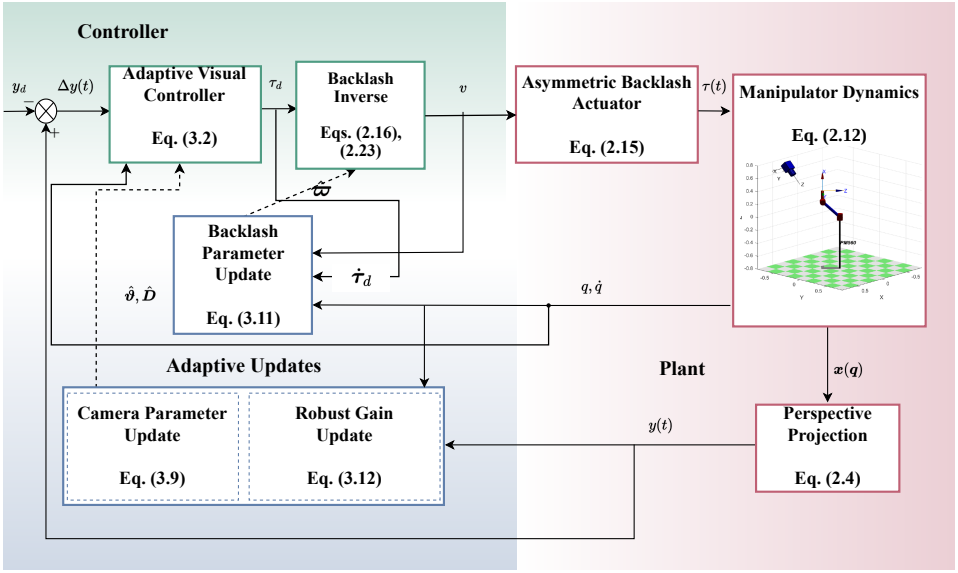


Figure 2. Control architecture for visual servoing with asymmetric actuator backlash.

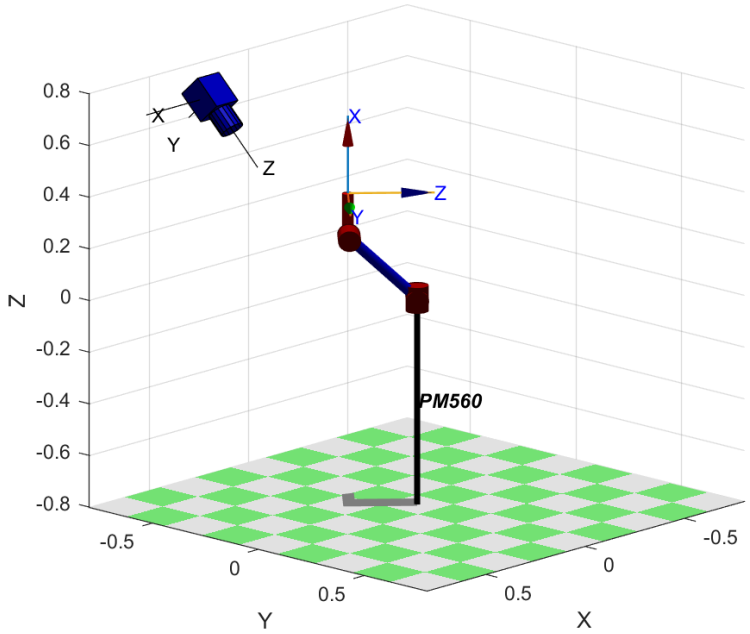


Figure 3. The robotic manipulator system with the fixed camera.

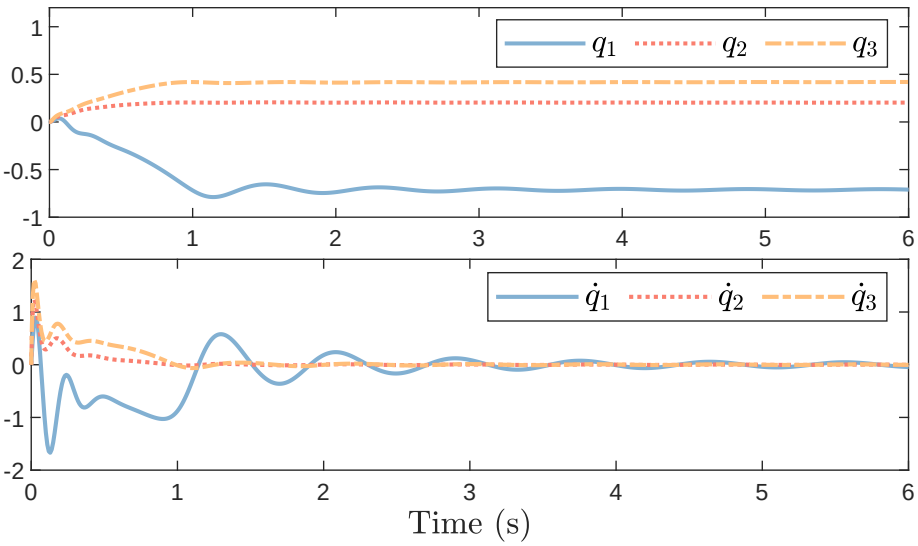


Figure 4. The robotic joint angle q and joint velocity $\dot{q}$ versus time.

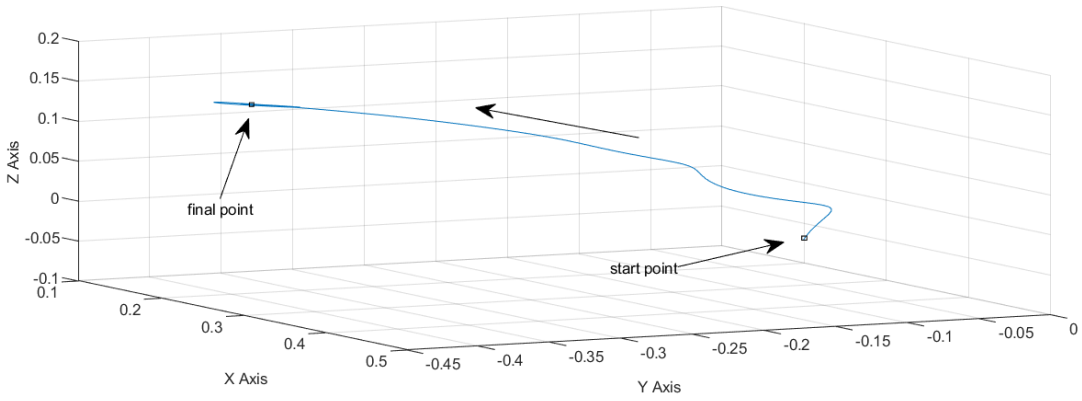


Figure 5. 3-D trajectory of feature points in three-dimensional space.

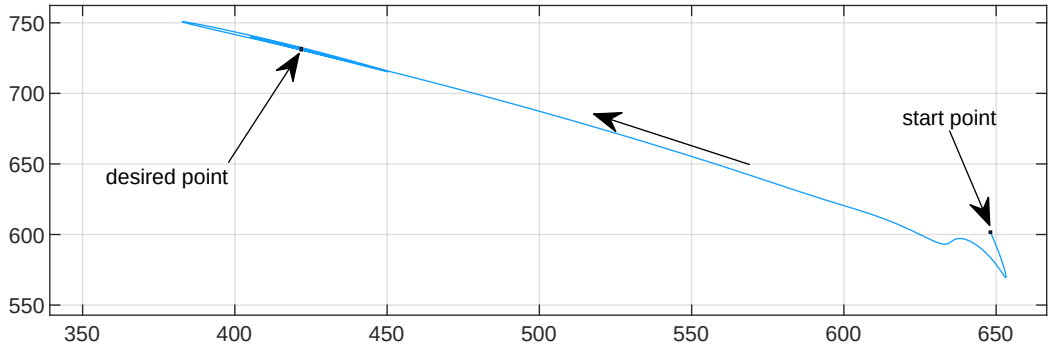


Figure 6. Image trajectory of feature points.

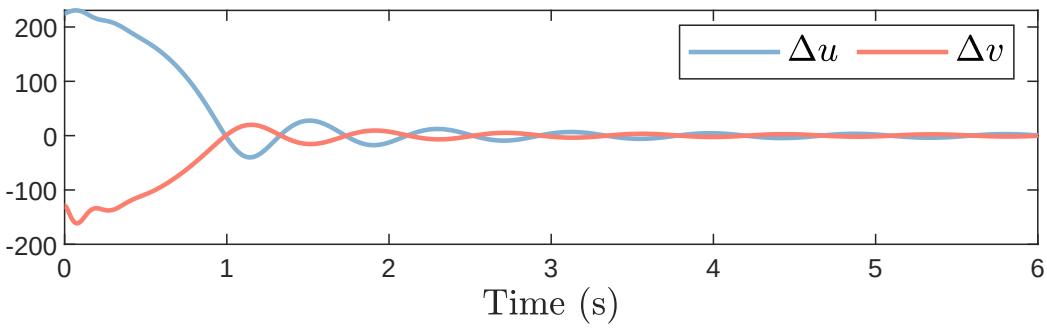


Figure 7. The image error $\Delta \boldsymbol{y}$ versus time.

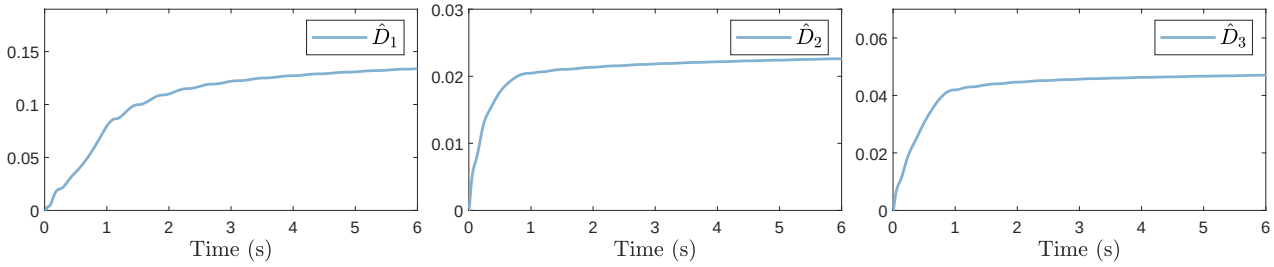


Figure 8. The adaptive robust parameters $\hat{\boldsymbol{D}}$ versus time.

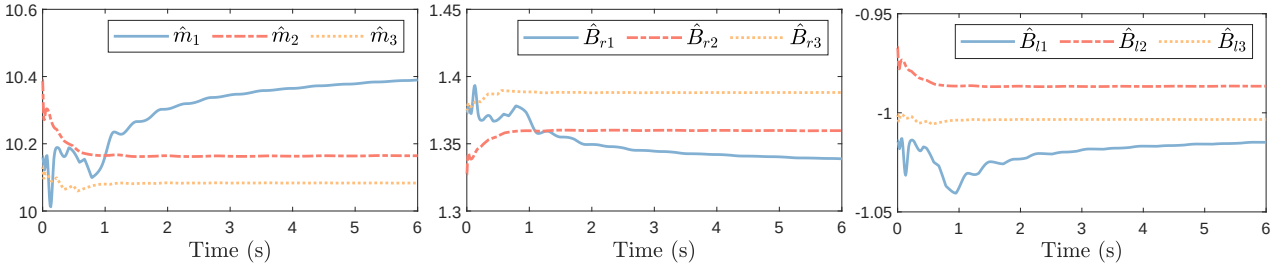


Figure 9. The adaptive parameters $\hat{m}$, $\hat{B}_r$, $\hat{B}_l$ versus time.

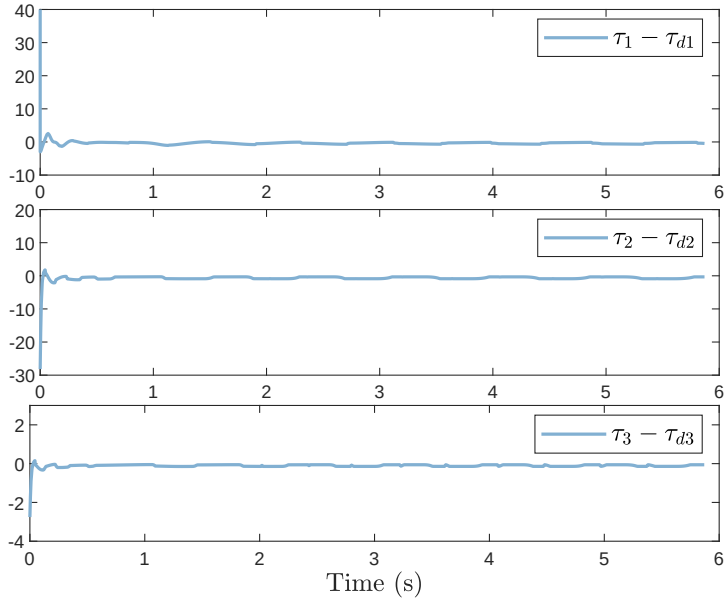


Figure 10. The torque tracking error $\boldsymbol{\tau} - \boldsymbol{\tau}_d$ of each joint versus time.

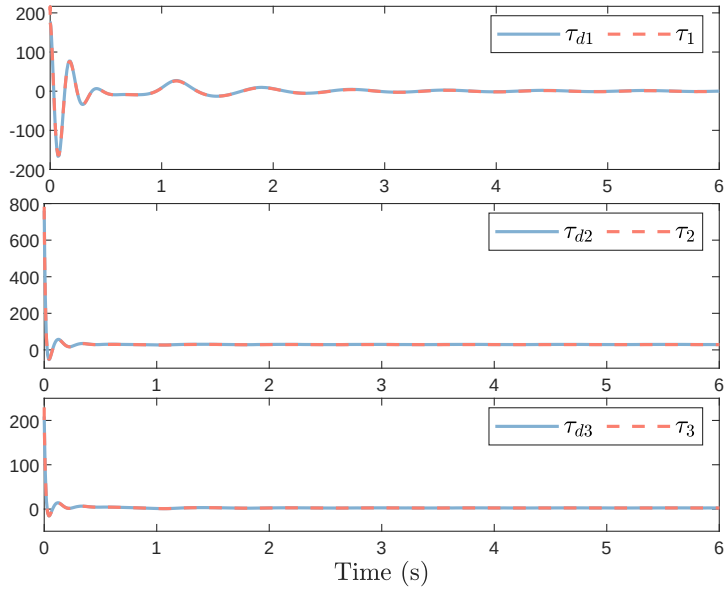


Figure 11. Actual torque output $\boldsymbol{\tau}$ and desired torque $\boldsymbol{\tau}_d$ of each joint versus time.

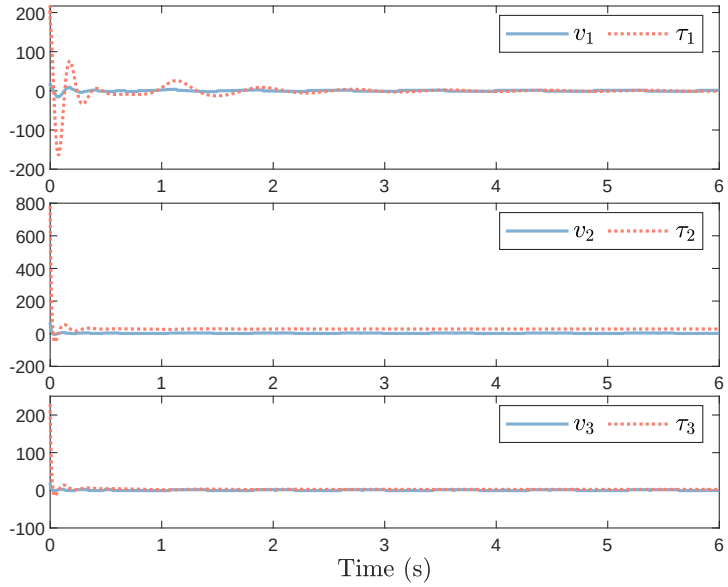


Figure 12. The input and output of the asymmetric backlash actuator versus time.

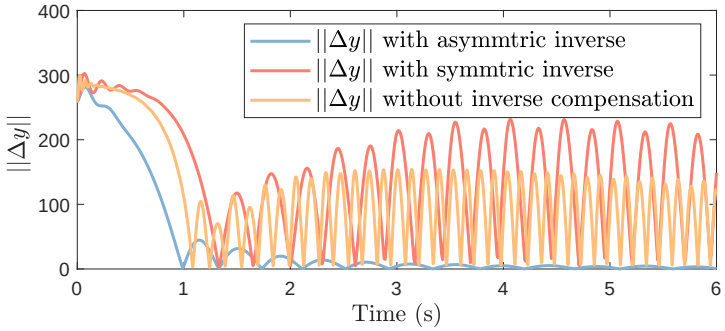


Figure 13. Comparison in terms of image error and convergence time.

The link offset and the link length of the ith link are denoted by d_i and a_i, and the link masses are $m_1 = 0$, $m_2 = 17.4$, and $m_3 = 4.8$. The simulated camera matrix is shown below with rounded entries, while the checks use the full-precision values stored in the simulation log.

$$\boldsymbol{M} = \begin{pmatrix} 750 & 362 & -362 & 281.9 \\ 0 & -168.3 & -892.4 & 506.9 \\ 0 & 0.7071 & -0.7071 & 0.9899 \end{pmatrix}. \tag{5.1}$$

The desired pixel coordinates are approximately $\boldsymbol{y}_{d,uv} = (422.7, 730.8)^T$ pixels. The controller uses the corresponding homogeneous target $\boldsymbol{y}_d = (u_d, v_d, 1)^T$. The physical backlash parameters are $m = m_r = 10$, $B_r = 1.4$, and $B_l = -1$. Thus, $\boldsymbol{\varpi} = (m, -mB_r, -mB_l)^T = (10, -14, 10)^T$, consistent with $B_r > 0 > B_l$. For the nominal continuous-feedback case, $\boldsymbol{\Upsilon} = \mathrm{diag}(3, 5, 2)$ and $\boldsymbol{\Xi} = 10\boldsymbol{I}_3$. The additional tests use the separate settings specified in Section 5.1.

For the nominal continuous-feedback case, the gains are

$$\boldsymbol{K}_1 = \mathrm{diag}(10, 380, 80), \qquad \boldsymbol{B} = 0.007\boldsymbol{I}_3,$$

$$\boldsymbol{\Gamma} = \mathrm{diag}(5 \times 10^{-4}\boldsymbol{I}_8, 50\boldsymbol{I}_3), \qquad \boldsymbol{K}_3 = 0.001\boldsymbol{I}_3.$$

A practical tuning guideline is to adjust $\boldsymbol{K}_1$ and $\boldsymbol{B}$ first for joint damping and image-error response, and then adjust $\boldsymbol{\Gamma}$ and $\boldsymbol{K}_3$ with the controller gains fixed. For fixed regressor and error signals, decreasing the diagonal entries of $\boldsymbol{\Gamma}$ increases the corresponding adaptation gain, while increasing $\boldsymbol{K}_3$ strengthens the stored-projection-error correction.

The projection conditions were evaluated along the recorded trajectories using the simulated ground-truth camera matrix. Table 2 reports the nominal case and the supplementary visual-feedback, offline-data, and comparison tests in Sections 5.1–5.2, including the numerical refinement checks. Every checked image point lies within the 1024×1024 image window. The minimum recorded depth is 0.586557 m and the minimum recorded singular value of $\boldsymbol{J}_v$ is 8.00333 pixels/rad. These checks concern the recorded time instants.

Figure 4 shows the joint-angle and joint-velocity responses in the nominal simulation.

The following results illustrate the regulation performance with backlash compensation. Figure 5 shows the trajectory of the end effector in the three-dimensional workspace, and Figure 6 shows the trajectory of the feature point on the image plane, which approaches the desired image position.

Figure 7 shows the image error decreasing to a small neighborhood of the target over the displayed interval. The result concerns image-space regulation; the image target alone does not prescribe a unique three-dimensional end-effector pose. Multi-feature pose regulation requires an extension of the present formulation.

Figures 8 and 9 show the evolution of the robust gains and inverse-parameter estimates. Figure 10 presents the torque compensation residual $\boldsymbol{\tau} - \boldsymbol{\tau}_d$, and Figure 11 compares the actual and desired joint torques. Figure 12 presents the actuator inputs v_i and outputs τ_i during the regulation task.

Figure 13 compares the image-error norm with the asymmetric inverse, the symmetric inverse, and without inverse compensation. With the asymmetric inverse, the oscillation amplitude decreases and the error approaches a small value by the end of the displayed interval. The two reference cases retain substantially larger oscillations over this interval. The nominal comparison illustrates the responses obtained with the initial estimates and stored data listed in Appendix A. The three cases share the initial joint state and image target, while their camera estimates and stored data are specified separately. Supplementary comparisons under finite-rate visual feedback, including module ablations and quantitative indices, are reported in Section 5.2.

Table 2. Projection-condition checks at recorded simulation instants. Ranges are reported for image coordinates and depth; the last row gives the smallest singular value observed.

Quantity	Nominal case	Supplementary cases	Units
u	[382.713, 653.295]	[254.844, 648.025]	pixels
v	[569.439, 750.821]	[585.420, 879.609]	pixels
${}^{c}z$	[0.599894, 0.883848]	[0.586557, 1.083848]	m
Minimum $\sigma_{\min}(\boldsymbol{J}_v)$	8.29707	8.00333	pixels/rad

5.1. Finite-rate visual feedback

Additional simulations use image acquisition at 120 Hz and control updates every 0.5 ms. Acquisition, image release, and control updates are scheduled separately. The controller uses the latest released image, held until a new frame becomes available. The commanded-torque rate is computed by backward difference at the control period and is shared by the inverse model and the backlash update. Actuator memory is updated at the same control instants, and the torque is held between them.

For reproducibility, the actuator output is initialized over $0 \le t_k < 1$ ms by

$$\tau_i[k] = \begin{cases} m_r(v_i[k] - B_r), & v_i[k] < 0, \\ m_l(v_i[k] - B_l), & v_i[k] \ge 0. \end{cases}$$

At $t_k \ge 1$ ms, the memory update in Section 2 is used with the most recently stored output and input. The first commanded-torque rate is set to zero; subsequent rates use the stated backward difference. This initialization is shared by all reported runs, and the 0–6 s metrics include the startup interval.

The simulations use MATLAB R2025a and the same three-joint Robotics Toolbox model, with $a_2 = 0.3318$ m and $a_3 = 0.1285$ m. The mechanical states are integrated between scheduled events by the fourth-order Runge–Kutta method with a maximum step of 0.25 ms. Over each control interval,

the linear camera-history term is integrated exactly with the other regressor input held; the backlash and robust updates include the stated control period. All additional cases use the fixed gains

$$K_1 = \mathrm{diag}(30, 380, 80), \qquad B = 0.004 I_3,$$
$$\Gamma = \mathrm{diag}(0.05 I_8, 5000 I_3), \qquad K_3 = I_3,$$
$$\Upsilon = \mathrm{diag}(3, 5, 2), \qquad \Xi = I_3.$$

The backlash parameters are $m_r = 10$, $m_l = 11$, $B_r = 1.4$, and $B_l = -1$, with $r = 10/11$ and $\kappa = 1000$. The robot starts from $q = \dot{q} = 0$ and $\hat{D} = 0$. The initial backlash parameter vectors and the full-precision configuration are supplied with the simulation files. The gains were selected in the baseline design stage and then held fixed across the comparisons.

The true camera has focal lengths of 750 pixels and a principal point of $(512, 512)$ pixels. Its nominal estimate uses focal lengths of $(825, 675)$ pixels, a principal point of $(522, 502)$ pixels, local x- and y-axis rotations of 5°, and a position offset of $(0.03, -0.03, 0.03)$ m. The estimated projection matrix is rescaled to the fixed-element convention of the 11-parameter representation. The alternative initialization halves this matrix error. Further cases move the camera backward by 0.20 m along its nominal optical axis or rotate it by 10° about its local y-axis; the desired pixels are the projections of the same target spatial point in each camera configuration.

The visual-channel tests add a 2-ms processing delay, zero-mean Gaussian noise with a standard deviation of 1 pixel per coordinate, and their combination. Noise also perturbs the five stored image observations; the desired image command remains fixed. The two noisy conditions use three fixed seeds, 20261006–20261008. A current-image reference provides the current projection at every control update without the additional 120 Hz image hold; its controller is still discrete.

Let $e_y(t) = y_{uv}(t) - y_{d,uv}$ and $e_p(t) = \pi(\hat{M}(t), x(t)) - y_{uv}(t)$, where π is perspective projection and y_{uv} is the noise-free simulated image. The interval root-mean-square (RMS) is

$$\mathrm{RMS}_{[a,b]}(e) = \left(\frac{1}{b-a} \int_a^b \|e(t)\|_2^2 \, dt \right)^{1/2}.$$

Full-run and final-second values use $[0, 6]$ s and $[5, 6]$ s. The latter is a fixed evaluation window, not an assumption of an exact steady state. Table 3 and Figure 14 show similar regulation errors for the baseline and the tested delay; pixel noise raises the final-second error to about 2.5 pixels. Camera initialization and geometry variations give 1.636–2.258 pixels. Reprojection errors are reported separately and are interpreted in the following subsection.

At the recorded samples, all features remain in the 1024×1024 image window; true depth ranges from 0.586557 to 1.083848 m across the tested cases. The smallest recorded singular value of the effective visual Jacobian is 8.003330 pixels/rad. Estimated projection denominators remain positive, and the maximum recorded actuator-input magnitude is $21.950337 < 25$. Halving the control period changes the baseline final-second regulation RMS from 1.714069 to 1.705512 pixels; halving only the mechanical integration step changes it by about 1.4×10^{-10} pixels. These checks concern the implemented numerical cases and do not extend the continuous-time proof to noisy or sampled-data asymptotic convergence.

Table 3. Additional visual-feedback tests. All RMS values are in pixels. Noisy cases report mean ± sample standard deviation over $n = 3$ runs; other cases are deterministic. All cases in this table retain the original five stored correspondences. Geometry changes also change the initial pixel error.

Condition	n	e_y RMS 0–6 s	e_y RMS 5–6 s	e_p RMS 5–6 s
Current-image reference	1	55.502	1.928	36.767
120-Hz baseline	1	55.898	1.714	36.786
Added 2-ms delay	1	56.123	1.706	36.808
Added 1-pixel noise	3	55.898 ± 0.101	2.498 ± 0.025	40.919 ± 6.186
Delay and noise	3	56.119 ± 0.103	2.496 ± 0.027	40.940 ± 6.185
Half initial camera error	1	55.378	1.636	18.844
Camera distance +0.20 m	1	45.034	2.258	26.564
Camera rotation 10°	1	57.695	1.812	40.789

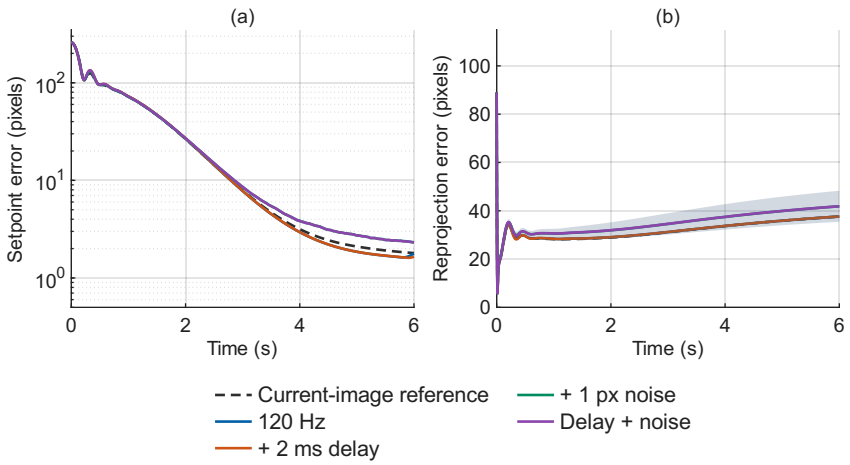


Figure 14. Effect of finite-rate feedback, delay, and pixel noise on (a) image-space regulation and (b) reprojection along the controlled trajectory. Noisy curves show the pointwise mean over three runs, with one standard deviation shaded. Statistics use the full-resolution records.

5.2. Supplementary comparisons and ablation tests

Figure 15 and Tables 4 and 5 compare five controller variants on the same asymmetric plant. The common settings are those of the noiseless 120-Hz baseline in Section 5.1, including the five offline correspondences, the camera estimate, $q(0) = \dot{q}(0) = 0$, and $\hat{D}(0) = 0$. The gains were selected in baseline-only tests of the full controller: the image gain was reduced to limit the initial actuator input, and damping and adaptation rates were then adjusted for the baseline response. They were frozen before the comparisons, with no method-specific retuning. The common initial inverse-parameter

vectors, written as columns, are

$$[\hat{\varpi}_1(0)\ \hat{\varpi}_2(0)\ \hat{\varpi}_3(0)] = \begin{bmatrix} 10.1626 & 10.3894 & 10.1332 \\ -13.9472 & -13.7883 & -13.9232 \\ 10.3055 & 10.0454 & 10.1405 \end{bmatrix},$$

where $\hat{\varpi}_i = (\hat{m}_{r,i}, -\hat{m}_{r,i}\hat{B}_{r,i}, -\hat{m}_{r,i}\hat{B}_{l,i})^T$; full-precision values are retained in the simulation files.

Table 4. Controller variants. The active gains are common to the supplementary variants; initial conditions are shared within each group.

Variant	Inverse	Backlash update	Robust term
Full	Asymmetric	On	On
Equal-slope inverse	$r_c = 1$	On	On
Robust only	Nominal gain	Off	On
Frozen parameters	Asymmetric	Off	On
No robust term	Asymmetric	On	Off

Table 5. Matched comparison and ablation results. Pixel RMS columns use 0–6 s and 5–6 s, respectively; torque indices use 0–6 s. The second group multiplies every initial physical backlash estimate $(\hat{m}_r, \hat{B}_r, \hat{B}_l)$ by 1.2 without changing the gains or camera settings.

Variant	Pixel RMS 0–6 s	Pixel RMS 5–6 s	t_s (s)	P_τ (N m)	R_τ (N m)	P_r (N m)
Initial backlash estimates specified above						
Full	55.898	1.714	4.7445	215.458	2.663	13.511
Equal-slope inverse	55.204	0.505	3.5155	225.137	2.374	13.176
Robust only	56.709	10.096	NA	226.928	15.805	19.771
Frozen parameters	55.556	1.417	4.4105	215.458	1.114	10.508
No robust term	55.885	2.368	NA	215.458	3.024	13.559
Initial physical backlash estimates multiplied by 1.2						
Full	60.291	6.702	NA	181.225	11.357	41.303
Frozen parameters	59.981	6.072	NA	181.225	10.575	41.303
No robust term	60.212	6.302	NA	181.225	11.388	41.303

The equal-slope variant sets $r_c = 1$ in both the inverse and its parameter-update regressor, while the plant retains $m_r = 10$ and $m_l = 11$. The variant with robust compensation only uses $v_i = \tau_{d,i}/\hat{m}_{r,i}(0)$, retaining the fixed nominal gain conversion and disabling the backlash update. The name *robust compensation only* refers to the backlash-compensation part of the controller. Freezing the inverse parameters removes only their update. Removing the robust term sets $\tau_0 = 0$ and disables its gain update. Camera adaptation is retained in every case. The equal-slope case is the $r_c = 1$ specialization of the same controller, so this comparison isolates compensation choices within a common architecture.

All runs last $T = 6$ s. Pixel RMS uses the definition in Section 5.1. With $r_\tau(t) = \tau(t) - \tau_d(t)$, the torque indices are

$$P_\tau = \max_{t\in[0,T]} \|\tau(t)\|_\infty, \qquad R_\tau = \left(\frac{1}{T}\int_0^T \|r_\tau(t)\|_2^2\, dt\right)^{1/2}, \qquad P_r = \max_{t\in[0,T]} \|r_\tau(t)\|_\infty.$$

The settling time t_s is the earliest recorded time for which $\|e_y(t)\|_2 \leq 2$ pixels at every remaining recorded instant through 6 s, with $6 - t_s \geq 1$ s. If this criterion is not met, the entry is NA (not attained). Integrals use the 0.5-ms records and trapezoidal quadrature; all extrema use the same records. These noiseless tests are deterministic, so the table reports individual runs without replicate-based uncertainty estimates. In all eight runs, the peak actual torque occurs at $t = 0$ under the initialization specified in Section 5.1; this index therefore reports the startup demand for that prescribed initialization.

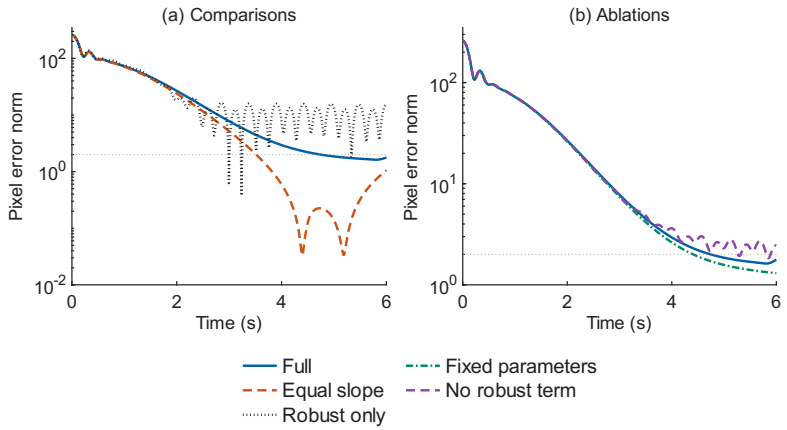


Figure 15. Supplementary sampled-data comparisons: (a) full controller, equal-slope inverse, and robust compensation only; (b) module ablations. The initial estimates and common settings are specified in this subsection; the horizontal dotted line denotes two pixels.

With the initial estimates specified above, the full controller gives a final-second pixel RMS of 1.714 pixels, compared with 10.096 pixels with robust compensation only and 2.368 pixels after removing the robust term. The corresponding compensation-residual RMS values are 2.663, 15.805, and 3.024 N m. The equal-slope and frozen-parameter variants give smaller final-second pixel errors, 0.505 and 1.417 pixels, respectively. In these supplementary baseline tests, the inverse reduces the final-second image error relative to robust compensation only, and the robust term improves this response within the full controller.

As an additional initialization-sensitivity check, all initial physical backlash estimates were multiplied by 1.2 in the three module variants; the camera settings and gains were unchanged. These three results are included in Table 5, and none meets the settling criterion within six seconds. Table 5 reports all outcomes for the stated initializations and evaluation windows, allowing the contributions of the compensation modules to be compared through the specified indices.

Remark 6. The inverse compensation and the backlash updates are formulated per joint, and the controller, the adaptive laws, and the Lyapunov function are stated for a general joint index. They are therefore not restricted to the three joints simulated here and extend directly to manipulators with more actuated joints; what changes is the dimension of the regressors and of the Jacobian, together with the computational cost. On the visual side, the rank condition of Assumption 4 must hold on the operating domain. A six-degree-of-freedom pose-regulation study remains a direction for further work. The present single-point objective leaves the end-effector posture and approach path unspecified. □

6. Conclusions

This paper presents an adaptive visual servoing scheme for manipulators with unknown asymmetric actuator backlash. A smooth inverse and adaptive robust compensation operate in parallel within the uncalibrated visual feedback loop. The analysis establishes boundedness, vanishing joint velocity, and finite limits of the joint configuration and image error on the stated operating domain. It also relates the limiting image error to the net residual torque: zero image error follows when the limiting feedback matrix has full column rank and the net-residual average vanishes. The task is single-point image-space setpoint regulation, without a prescribed three-dimensional end-effector pose. Simulations illustrate the regulation performance. The following directions remain open:

1) Fixed time control. The current analysis provides conditions for asymptotic regulation but does not prescribe a convergence time. A fixed-time formulation would provide a settling-time bound independent of the initial state.
2) Trajectory tracking. Extending the current framework from setpoint regulation to dynamic trajectory tracking is essential for enhancing the manipulator's utility in complex tasks such as welding, drawing, or inspection.

Appendix A. Settings of the nominal comparison

The three cases in Figure 13 use continuous visual feedback, $q(0) = \dot{q}(0) = 0$, the same true camera, and the target of $(422.7332, 730.8445)^T$ pixels. The common gains K_1, B, Γ, and K_3 are given in Section 5. The true backlash parameters are $m_r = 10$, $m_l = 11$, $B_r = 1.4$, and $B_l = -1$. The saved initial camera estimates, reconstructed using the fixed element $M_{34} = 0.9899495$, are

$$\hat{M}_a(0) = \begin{bmatrix} 756.9989 & 362.7267 & -355.4942 & 289.0377 \\ 6.3853 & -165.0954 & -888.2926 & 516.5406 \\ 0.3360 & 6.0157 & 7.4927 & 0.9899 \end{bmatrix},$$

$$\hat{M}_s(0) = \hat{M}_n(0) = \begin{bmatrix} 759.1338 & 364.8237 & -352.3898 & 291.4258 \\ 6.3236 & -162.8226 & -890.7926 & 511.7079 \\ 0.9754 & 10.2822 & 8.9988 & 0.9899 \end{bmatrix}.$$

Here a, s, and n denote the asymmetric-inverse, symmetric-inverse, and uncompensated cases. Their stored spatial positions, in meters and arranged as columns, are

$$X_a = \begin{bmatrix} 0.46030 & 0.15371 & 0.30621 & 0.39961 & 0.23581 \\ -0.15005 & -0.08452 & -0.04635 & -0.05961 & -0.05610 \\ 0.00000 & -0.42266 & -0.35586 & -0.25695 & -0.39774 \end{bmatrix},$$

$$X_s = X_n = \begin{bmatrix} 0.46030 & 0.15371 & 0.17635 & 0.15732 & 0.46146 \\ -0.15005 & -0.08452 & -0.07483 & -0.08288 & -0.14608 \\ 0.00000 & -0.42266 & -0.41825 & -0.42209 & -0.01025 \end{bmatrix}.$$

Each stored pixel pair is the projection of its spatial position under the common true camera. The full-precision values are retained in the accompanying nominal-comparison settings file.

The initial physical inverse estimates $(\hat{m}_i, \hat{B}_{r,i}, \hat{B}_{l,i})^T$, arranged as columns, are

$$P_a(0) = \begin{bmatrix} 10.1626 & 10.3894 & 10.1332 \\ 1.3724 & 1.3271 & 1.3740 \\ -1.0141 & -0.9669 & -1.0007 \end{bmatrix}, \qquad P_s(0) = \begin{bmatrix} 10.0071 & 10.0396 & 10.0018 \\ 1.4211 & 1.4480 & 1.4425 \\ -0.9542 & -0.9672 & -0.9533 \end{bmatrix}.$$

The nominal asymmetric implementation uses the reparameterized estimates with diagonal update weight $\mathrm{diag}(3, 5, 2)$; the archived symmetric implementation updates the physical parameters with diagonal weight $\mathrm{diag}(200, 100, 100)$. Both start with $\hat{D}(0) = 0$ and use $\Xi = 10I_3$. The nominal inverse and parameter-update weighting coefficients are 10^8 and 10^3, respectively. The symmetric inverse uses equal branch slopes, while the plant remains asymmetric. In the uncompensated case, $v_i = \tau_{d,i}$ and the robust term is absent.

These are the recorded settings of the nominal responses. Section 5 provides the gain-tuning guideline. Section 5.2 reports the additional comparisons with common initial estimates, stored data, and active gains, selected using the full-controller baseline and then fixed for all variants.

Data availability

The data that support the findings of this study are available from the corresponding author upon reasonable request.

Author contributions

Rong Lu: Conceptualization, methodology, software, writing – original draft, funding acquisition, writing – review & editing; Jianlan Guo: Supervision, project administration, funding acquisition, writing – review & editing; Guanyu Lai: Methodology, validation, writing – review & editing; Haoxu Shi: Software, data curation, writing – review & editing; Xiaohang Su: Investigation, formal analysis, writing – review & editing. All authors have read and approved the final version of the manuscript for publication.

Use of Generative-AI tools declaration

The authors declare they have not used Artificial Intelligence (AI) tools in the creation of this article.

Acknowledgments

This work was supported by the Guangdong Provincial Department of Education: the 2025 Characteristic Innovation Project of General Higher Education Institutions (No. 2025KTSCX373), the 2026 Guangdong Provincial Education Science Planning Project (Higher Education Special Program) (No. 2026GXJK0878), the 2024 Educational Science Planning Project (Higher Education Special Project) (No. 2024GXJK1182), and the Innovative Team Project of General Universities in Guangdong Province (No. 2025KCXTD094). Additional funding was provided by the Guangdong Provincial Philosophy and Social Science Planning Project (No. GD25CSH06) and the 2026–2027 Research Project on Scientific and Technological Innovation and the Development of Sports Culture (No. GDSS2026N170).

Conflict of interest

All authors declare no conflicts of interest in this paper.

References

1. M. Kharrat, M. Krichen, L. Alkhalifa, K. Gasmi, Neural networks-based adaptive command filter control for nonlinear systems with unknown backlash-like hysteresis and its application to single link robot manipulator, *AIMS Math.*, **9** (2024), 959–973. https://doi.org/10.3934/math.2024048
2. M. Staniak, C. Zieliński, Structures of visual servos, *Robot. Auton. Syst.*, **58** (2010), 940–954. https://doi.org/10.1016/j.robot.2010.04.004
3. H. Zhong, W. Wen, J. Fan, W. Yang, Reinforcement learning-based adaptive tracking control for flexible-joint robotic manipulators, *AIMS Math.*, **9** (2024), 27330–27360. https://doi.org/10.3934/math.20241328
4. Y. Wang, W. Zhang, H. Wen, *Position-based visual servo control for robotic manipulation of space structures*, In: International Conference on Mechanical System Dynamics, Springer, 2023, 2435–2443. https://doi.org/10.1007/978-981-99-8048-2_167
5. S. Zhou, C. Shen, F. Pang, Z. Chen, J. Gu, S. Zhu, Position-based visual servoing control for multi-joint hydraulic manipulator, *J. Intell. Robot. Syst.*, **105** (2022), 33. https://doi.org/10.1007/s10846-022-01628-x
6. J. Li, H. Xie, K. H. Low, J. Yong, B. Li, Image-based visual servoing of rotorcrafts to planar visual targets of arbitrary orientation, *IEEE Robot. Autom. Lett.*, **6** (2021), 7861–7868. https://doi.org/10.1109/LRA.2021.3101878
7. X. Zhang, Y. Fang, X. Zhang, J. Jiang, X. Chen, Dynamic image-based output feedback control for visual servoing of multirotors, *IEEE T. Indu. Inform.*, **16** (2020), 7624–7636. https://doi.org/10.1109/tii.2020.2974485
8. Y. Chen, Y. Wu, Z. Zhang, Z. Miao, H. Zhong, H. Zhang, et al., Image-based visual servoing of unmanned aerial manipulators for tracking and grasping a moving target, *IEEE T. Indu. Inform.*, **19** (2022), 8889–8899. https://doi.org/10.1109/TII.2022.3222688
9. Q. Song, R. Lu, Y. Long, X. Zheng, A calibration-free visual control approach for table tennis training robots using a positional monocular camera, *AIMS Math.*, **10** (2025), 27364–27380. https://doi.org/10.3934/math.20251203
10. X. Yang, J. Wang, S. Song, M. Q. H. Meng, Model-free and uncalibrated eye-in-hand visual servoing approach for concentric-tube robots, *IEEE T. Instrum. Meas.*, **71** (2022), 1–11. https://doi.org/10.1109/TIM.2022.3147867
11. X. Ren, H. Li, Uncalibrated image-based visual servoing control with maximum correntropy Kalman filter, *IFAC-PapersOnLine*, **53** (2020), 560–565. https://doi.org/10.1016/j.ifacol.2021.04.200
12. N. Tan, P. Yu, W. Zheng, Uncalibrated and unmodeled image-based visual servoing of robot manipulators using zeroing neural networks, *IEEE T. Cybernetics*, **54** (2022), 2446–2459. https://doi.org/10.1109/TCYB.2022.3227470

13. Y. H. Liu, H. Wang, W. Chen, D. Zhou, Adaptive visual servoing using common image features with unknown geometric parameters, *Automatica*, **49** (2013), 2453–2460. https://doi.org/10.1016/j.automatica.2013.04.018

14. C. C. Cheah, C. Liu, J. J. E. Slotine, *Adaptive vision based tracking control of robots with uncertainty in depth information*, In: Proceedings of the 2007 IEEE International Conference on Robotics and Automation, 2007, 2817–2822. https://doi.org/10.1109/ROBOT.2007.363898

15. Y. H. Liu, H. Wang, C. Wang, K. K. Lam, Uncalibrated visual servoing of robots using a depth-independent interaction matrix, *IEEE T. Robot.*, **22** (2006), 804–817. https://doi.org/10.1109/TRO.2006.878788

16. G. Lai, A. Liu, W. Yang, Y. Chen, L. Zhao, Uncalibrated adaptive visual servoing of robotic manipulators with uncertainties in kinematics and dynamics, *Actuators*, **12** (2023), 143. https://doi.org/10.3390/act12040143

17. C. Cai, E. Dean-León, D. Mendoza, N. Somani, A. Knoll, *Uncalibrated 3d stereo image-based dynamic visual servoing for robot manipulators*, In: 2013 IEEE/RSJ International Conference on Intelligent Robots and Systems, 2013, 63–70. https://doi.org/10.1109/IROS.2013.6696333

18. Z. Zhao, Z. Tan, Z. Liu, M. O. Efe, C. K. Ahn, Adaptive inverse compensation fault-tolerant control for a flexible manipulator with unknown dead-zone and actuator faults, *IEEE T. Indu. Electron.*, **70** (2023), 12698–12707. https://doi.org/10.1109/TIE.2023.3239926

19. G. Shao, X. F. Wang, R. Wang, A distributed strategy for games in Euler–Lagrange systems with actuator dead zone, *Neurocomputing*, **560** (2023), 126844. https://doi.org/10.1016/j.neucom.2023.126844

20. R. Zhang, H. Ji, *Robust adaptive trajectory tracking control for uncertain quadrotor unmanned aerial vehicles in the presence of actuator saturation*, In: 2020 5th International Conference on Control and Robotics Engineering, 2020, 104–108. https://doi.org/10.1145/3424311.3424325

21. J. H. An, H. S. Kim, Interval type-2 fuzzy-model-based sampled-data control of an AUV depth system with input saturation, *Actuators*, **13** (2024), 71. https://doi.org/10.3390/act13020071

22. Z. Shi, Z. Zuo, Backstepping control for gear transmission servo systems with backlash nonlinearity, *IEEE T. Automat. Sci. Eng.*, **12** (2015), 752–757. https://doi.org/10.1109/TASE.2014.2369430

23. H. Yonezawa, A. Yonezawa, I. Kajiwara, Efficient tuning scheme of mode-switching-based powertrain oscillation controller considering nonlinear backlash, *IEEE Access*, **11** (2023), 93935–93947. https://doi.org/10.1109/ACCESS.2023.3310540

24. X. He, Z. Zhao, J. Su, Q. Yang, D. Zhu, Adaptive inverse control of a vibrating coupled vessel-riser system with input backlash, *IEEE T. Syst Man Cyb.-S.*, **51** (2021), 4706–4715. https://doi.org/10.1109/TSMC.2019.2944999

25. L. Kong, Q. Lai, Y. Ouyang, Q. Li, S. Zhang, Neural learning control of a robotic manipulator with finite-time convergence in the presence of unknown backlash-like hysteresis, *IEEE T. Syst. Man Cy.-S.*, **52** (2022), 1916–1927. https://doi.org/10.1007/s40278-022-19511-1

26. Z. Yin, W. He, O. Kaynak, C. Yang, L. Cheng, Y. Wang, Uncertainty and disturbance estimator-based control of a flapping-wing aerial vehicle with unknown backlash-like hysteresis, *IEEE T. Indu. Electron.*, **67** (2020), 4826–4835. https://doi.org/10.1109/TIE.2019.2926055

27. J. Zhao, Y. Li, Y. Cao, F. Zhang, M. Cui, R. Xu, High-precision position tracking control with a hysteresis observer based on the Bouc–Wen model for smart material-actuated systems, *Actuators*, **13** (2024), 105. https://doi.org/10.3390/act13030105

28. N. Xu, S. Yue, N. Zhao, B. Niu, X. Zhao, SMS-based optimal control of completely unknown nonlinear systems with unknown actuator saturation, *Int. J. Adapt. Control.*, **40** (2026), 1956–1971. https://doi.org/10.1002/acs.70109

29. Z. Wu, N. Zhao, A. A. Albeshri, Deferred actuator replacement-based performance recovery consensus control for nonlinear multi-agent systems under DoS attacks, *Nonlinear Dynam.*, **114** (2026), 865. https://doi.org/10.1007/s11071-026-12682-7

30. X. Chen, L. Ma, X. Zhao, G. Zong, Predefined-time sliding-mode formation control for second-order nonlinear multi-agent systems under deception attacks, *Eur. J. Control*, **91** (2026), 101534. https://doi.org/10.1016/j.ejcon.2026.101534

31. G. Tao, Adaptive backlash compensation for robot control, *IFAC Proc. Volumes*, **29** (1996), 5244–5249. https://doi.org/10.1016/S1474-6670(17)58514-6

32. J. Zhou, C. Zhang, C. Wen, Robust adaptive output control of uncertain nonlinear plants with unknown backlash nonlinearity, *IEEE T. Automat. Control*, **52** (2007), 503–509. https://doi.org/10.1109/TAC.2006.890473

33. F. Wang, L. Song, Z. Liu, *Image-based visual servoing control for robot manipulator with actuator backlash*, In: 2016 3rd International Conference on Informative and Cybernetics for Computational Social Systems, 2016, 272–276. https://doi.org/10.1109/iccss.2016.7586464

34. S. Mirshahzadeh, H. Khodadadi, Feedback linearization controller design for a geared transmission system considering asymmetric backlash and friction, *J. Simul. Anal. Novel Technol. Mech. Eng.*, **15** (2023), 15–26. https://doi.org/10.1002/citp.202370709

35. J. Liu, Y. Sun, Z. Liu, Y. Gao, L. Wu, J. I. Leon, et al., Predefined-time reliable control for robotic systems with prescribed performance, *IEEE T. Ind. Electron.*, **72** (2025), 11695–11703. https://doi.org/10.1109/TIE.2025.3558003

36. Z. Liu, O. Zhang, Y. Zhao, Q. Zhu, J. Liu, Adaptive neural network-based fixed-time control for robots with input saturation and prescribed performance, *Nonlinear Dynam.*, **113** (2025), 18229–18241. https://doi.org/10.1007/s11071-025-11103-5



AIMS Press

© 2026 the Author(s), licensee AIMS Press. This is an open access article distributed under the terms of the Creative Commons Attribution License (https://creativecommons.org/licenses/by/4.0)